Advances in Computational Design, *Vol. 10, No. 1 (2025) 1-34*
https://doi.org/10.12989/acd.2025.10.1.001

Critical buckling analysis of functionally graded porous beam using Karush-Kuhn-Tucker conditions

Geetha Narayanan Kannaiyan*[1], Vivekanandam Balasubramaniam[2],
Bridjesh Pappula[3] and Seshibe Makgato[3]

[1]Department of Mathematics, Dayananda Sagar College of Engineering, Bengaluru 560078, India
[2]Faculty of Computer Science and Multimedia, Lincoln University College, Malaysia
3Department of Chemical & Materials Engineering, College of Science,
Engineering and Technology, University of South Africa (UNISA),
c/o Christiaan de Wet & Pioneer Avenue, Florida Campus 1710, Johannesburg, South Africa

(Received August 29, 2023, Revised December 25, 2024, Accepted January 2, 2025)

Abstract. Functionally graded porous beams (FGPB) are structural components engineered to enhance mechanical performance by customized material gradation and porosity distribution. The present study examines the buckling analysis of FGPB modelled using Higher-order shear deformation theory. The governing equations are formulated via Hamilton's principle and solved utilizing Karush-Kuhn-Tucker conditions. The analysis utilizes gradient indices (P_x, P_z), porosity distributions (even and uneven) and porosity indices to assess their influence on the dimensionless critical buckling loads under various boundary conditions, including Simply Supported (SS), Clamped-Simply supported (CS), Clamped-Clamped (CC), and Clamped-Free (CF). In line with this, the results show that an increase in P_x led to a decrease in the buckling load from 51.342 when P_x=0 to 8.811 when P_x=5 under the SS boundary conditions. Likewise, with increase in P_z the buckling load was reduced from 51.342 to 13.351. Uneven porosity consistently exhibited higher dimensionless critical buckling as compared to even porosity. Under CC boundary conditions, the dimensionless critical buckling load was 151.970 and 196.587 for even and uneven porosity distribution at P_x=0 and P_z=0. Among the boundary conditions, CC demonstrated the highest stability, with a dimensionless critical buckling load of 151.970, succeeded by CS (101.656), SS (51.342), and CF (13.175). These results prove the ability of the outlined methodology with errors less than 5% compared to literature. This study emphasizes the significance of material gradation and porosity in structural stability and presents a comprehensive method for designing innovative lightweight structures. Future studies may consider Machine Learning based predictive modeling for complex geometries.

Keywords: aspect ratio; dimensionless critical buckling; functionally graded porous beam; gradient index; higher order shear deformation theory; Karush-Kuhn-Tucker conditions; porosity

1. Introduction

The continuous advancement of technology intensifies the demand for diverse features inside a single component, rendering it challenging or unfeasible for a single material to fulfill all requisite

---

*Corresponding author, Professor, E-mail: nkgeeth@gmail.com

http://www.techno-press.org/?journal=acd&subpage=7 ISSN: 2383-8477 (Print), 2466-0523 (Online)

properties. The combination of two or more materials is an optimal strategy to leverage the unique properties of each material. Functionally Graded Materials (FGM) represents a type of composite, characterized by the presence of distinct materials at various locations inside a single component, resulting in a gradient of qualities such as chemical, physical, and mechanical properties (Miyamoto *et al*. 1999). Out of these FGM, Functionally Graded Porous Structures (FGPS) stand out for their lightweight nature that exhibit enhanced mechanical properties and adaptability to diverse engineering needs (Chintalapudi *et al*. 2024). These materials find extensive applications in aerospace (Zhai *et al*. 2024), biomedical implants (Lore *et al*. 2024), and energy systems (Chen *et al*. 2023), where their tailored properties enable optimal performance under challenging conditions.

The study of the mechanical properties of FGPS has become increasingly important due to the increasing complexity and variety of their applications (Qui *et al*. 2023). The beam element composed of FGPS, Functionally Graded Porous Beams (FGPB), has gained significant interest from researchers due to its critical importance in engineering applications over the past several decades (Zheng *et al*. 2024). Buckling represents a critical mode of structural instability where components under compressive loads experience sudden lateral deformation that potentially lead to catastrophic failure. This phenomenon becomes especially pronounced in materials designed for optimized performance, such as FGM and FGPB because of their tailored material properties and spatial heterogeneity (Ghatage *et al*. 2020). Comprehensive investigations have been made into the buckling response of FGPB through conventional and theoretical techniques to capture the relationship between material variation, porosity distribution and the corresponding critical buckling loads.

To study the non-dimensional critical buckling loads in FGPB, Turan *et al*. (2024) used parabolic shear deformation theory based on Finite Element Method (FEM) under various boundary conditions. They found that both the overall quantity of pores and their locations are significant factors influencing the crucial buckling loads. For low gradation exponents, the specific type of porosity does not considerably influence the variation in critical buckling loads. (Chintalapudi *et al*. 2024) considered the structural analysis of Functionally Graded Beams (FGB) using Vogel's approximation under various boundary conditions. (Xu *et al*. 2024) proposed a multiscale analytical approach to investigate the buckling behavior of FGB composed of microstructurally tunable materials adapting Timoshenko Bean Theory (TBT). The analytical equations were derived using Ritz method for different boundary conditions. (Sun *et al*. 2024) adapted consistent shear beam theory to assess the vibration analysis of FGB based on the physical neutral plane. (Nguyen *et al*. 2024) studied the buckling and vibration analysis of FGPB and laminated composite. The governing equations were developed from the Lagrange principle and Legendre-Ritz functions were employed to solve these equations for both symmetric and asymmetric configurations. Higher-Order Shear Deformation Theory (HSDT) has been adopted to achieve a more realistic representation of transverse shear stresses (Yaylacı *et al*. 2022, Nguyen *et al*. 2023). HSDT, such as Reddy's HSDT provide non-linear stress distributions that enable detailed investigations of buckling loads and stress profiles in complex loading scenarios (Bridjesh *et al*. 2024, Nguyen *et al*. 2024).

Analytical solutions are formulated to examine the static and dynamic behavior of FGB, considering their simplicity and explicit nature. (Wu *et al*. 2024) compared the buckling and vibration analysis of FGPB using classical beam theory, first-order shear deformation theory, third-order shear deformation theory, and broken-line hypothesis-based shear deformation beam theory. The governing equations associated with these beam theories were derived using

Hamilton's principle and the generalized differential quadrature method was used to solve them. Non- local strain gradient theory integrated with HSDT was used by (Liang *et al*. 2024) to conduct the non-linear isogeometric analysis on curved beams. (Mesbah *et al*. 2024) implemented Quasi-3Q finite element model based on shear and normal deformation beam theory to assess the vibration and bending analysis of an FGB. The governing equations were derived using weak version of variational principles. Couple stress theory includes rotational effects and size dependency through a couple stress tensors that enable accurate modeling of small-scale structures (Wu and Huang 2024, Deng and Shang 2024, Taghizadeh *et al*. 2024). It captures microstructural behaviors and is particularly useful for micro/nano-scale materials and functionally graded structures (Indronil 2024, Wang *et al*. 2024).

The structural analysis of FGB entails resolving governing equations that incorporate spatially variable material properties. The equations are exceedingly complex because of the non-homogeneous characteristics of FGB. Various solution methodologies have been devised to effectively handle these difficulties. Analytical approaches provide closed-form solutions for geometries that exhibit diverse loading conditions and different boundary conditions. Laplace transforms, and Fourier series expansions have been employed to resolve the governing differential equations of FGB. Their applicability is limited to relatively simple problems and as the complexity of material gradation and loading often renders the equations unsolvable in closed form.

Static and dynamic problems related to structural components can be described by higher-order partial differential equations. The researchers have long been engaged in exploring various solution strategies to solve the governing equations in the structural analysis of FGB. The Galerkin (Ma *et al*. 2024, Amandeep *et al*. 2024) and Rayleigh-Ritz methods (Kumar *et al*. 2024, Rajasekaran 2024) are widely used to solve the governing equations. These techniques estimate the solution by representing the displacement field as a series of trial functions that are in accordance with the boundary conditions (Le *et al*. 2024). It was observed by (Patil *et al*. 2024) that the Rayleigh-Ritz technique minimizes the total potential energy and (Jain *et al*. 2024) noticed that the Galerkin method employs weighted residuals to ensure the governing equations are satisfied. Various methods have been employed to solve the governing equations of the structural analysis of FGB. Semi-analytical and numerical solutions are developed not only to alleviate computing challenges but also to address these problems effectively. Numerical methods have also been widely used for solving governing equations in FGB analysis (Benmalek *et al*. 2024). (Chen *et al*. 2024) and Hasim and Kefal (2024) ascertained that the Mesh-free methods and isogeometric analysis have also been employed to overcome the limitations of traditional FEM in capturing steep material gradients. Additionally, researchers have adequately examined traditional numerical methods to analyze structural static and dynamic problems. Perturbation methods provide approximate solutions by expanding the governing equations into a series of terms based on a small parameter (Chandel and Talha 2024, Amir and Kim 2024). These methods are particularly useful for analyzing slightly nonlinear problems. Modifications in approximations or algorithms enhance the computing efficiency of numerical approaches in addressing complex issues. Variational methods use principles like the principle of minimum potential energy to derive approximate solutions (Yu 2024, Kumar *et al*. 2024).

HSDT demonstrates accuracy in assessing the mechanical behavior of thick FGB as shear deformation and rotary inertia are considered. The methodologies for analyzing governing equations in FGPBs encounter numerous basic limitations. Analytical approaches frequently do not yield solutions for geometries with complex boundary and loading conditions. Numerical approaches necessitate considerable computational resources to accurately predict steep material gradients and porosity distributions. Computational demand increases exponentially for HSDTs when dealing with coupled phenomena like thermo-mechanical effects. Semi-analytical methods struggle to generalize solutions across diverse configurations that require extensive customization for specific boundary conditions. They may introduce approximation errors for complex geometries and nonlinear material gradations.

The governing equations are highly nonlinear due to the coupling of material gradation, porosity distribution, and boundary conditions. Under complex loading conditions, conventional solution methods may fail to capture the full interaction, and the unified framework that incorporates the multiple factors affecting buckling behavior is limited. The novelty of the present study is in solving the governing equations using Karush-Kuhn-Tucker (KKT) conditions. Applying the buckling analysis as a constrained optimization problem gives a systematic technique for determining the critical buckling loads with various combinations of boundary conditions and material gradation profiles.

The aim of the present study is to establish a comprehensive mathematical framework for examining the buckling analysis of an FGPB utilizing HSDT. The study entails the development of a FGPB mathematical model employing the power law to depict material homogeneity for both uniform and non-uniform porosity distributions. The governing equations are derived using Hamilton's principle which incorporates potential energy terms and displacement work and are solved in a systematic manner using KKT conditions. This methodology is also used to study various boundary conditions including Simply Supported (SS), Clamped Simply Supported (CS), Clamped Clamped (CC) and Clamped Free (CF). Dimensionless critical buckling loads are computed for various parameters including gradient indices, aspect ratios and porosity indices to gain a deeper understanding of the buckling behavior of FGPB.

2. Materials and methods

2.1 Formulation of functionally graded porous beam

In the present study, an FGPB is modelled with a metal-ceramic material combination with spatially varying properties along its cross-section. The FGPB has a rectangular cross-section with a width b, height h, and length L. The material properties vary continuously from the ceramic-rich bottom surface to the metal-rich top surface that follows a power-law distribution, as shown in Fig. 1. This gradation allows the beam to combine the strength of ceramics with the ductility of metals to optimize its structural performance under compressive loads (Karamanli 2018). The porosity distribution in the beam is represented as even and uneven, as illustrated in Fig. 1. The pores have even distribution over the cross-section in the case of even porosity, demonstrating consistent material properties and in uneven porosity circumstances, the pores are concentrated in certain places, resulting in local changes in stiffness and density (Geetha *et al*. 2023). These configurations are vital since they influence the fundamental buckling load and overall stability of the beam. The beam experiences a compressive load (q_x) along its length, with the x-axis denoting the longitudinal direction, the z-axis indicating the vertical direction, and the y-axis representing the transverse direction. The upper surface is mostly metallic, while the lower surface is mainly ceramic, facilitating a graded transition of material characteristics to withstand elevated thermal and mechanical stresses.

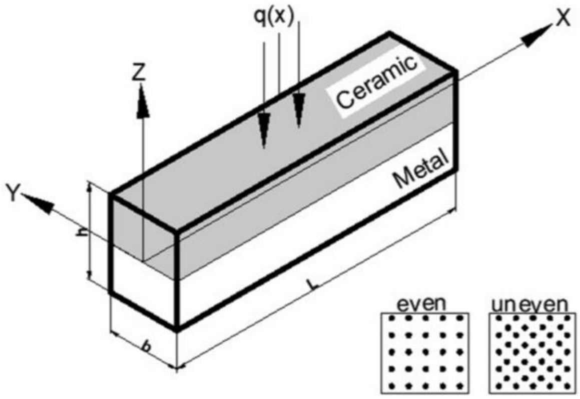

Fig. 1 The geometry of functionally graded porous beam exhibiting even and uneven porosity distribution

2.2 Material composition and properties

The material composition of the FGPB is defined using volume fractions that describe the spatial variation of constituent materials (metal and ceramic) throughout the beam. Eqs. (1)-(2) represents the volume of the beam (Karamanli 2018).

$$V_f = V_{f1} + V_{f2} = 1 \tag{1}$$

$$V_{f1}(x,z) = \left(\frac{z}{h} + \frac{1}{2}\right)^{P_z} \left(\frac{x}{L} + \frac{1}{2}\right)^{P_x} \tag{2}$$

here, V_f is the volume of the beam, V_{f1} is the volume fraction of the ceramic phase and V_{f2} is the volume fraction of metallic phase. P_z is the gradient index in the vertical direction, P_x is the gradient index in the longitudinal direction. 'z' and 'x' represent the spatial position within the beam. $\left(\frac{x}{L} + \frac{1}{2}\right)^{P_x}$ and $\left(\frac{z}{h} + \frac{1}{2}\right)^{P_z}$ governs the material variation along the vertical and longitudinal directions, respectively. The spatial variation of physical and mechanical properties due to the gradation of material composition in the FGPB with even and uneven porosity distributions are shown in Eqs. (3)-(4), respectively (Nguyen *et al*. 2022).

$$P(x,z) = (P_c - P_m)\left(\frac{z}{h} + \frac{1}{2}\right)^{P_z} \left(\frac{x}{L} + \frac{1}{2}\right)^{P_x} + P_m - \frac{\alpha}{2}(P_c + P_m) \tag{3}$$

$$P(x,z) = (P_c - P_m)\left(\frac{z}{h} + \frac{1}{2}\right)^{P_z} \left(\frac{x}{L} + \frac{1}{2}\right)^{P_x} + P_m - \frac{\alpha}{2}(P_c + P_m)\left(1 - \frac{2|z|}{h}\right) \tag{4}$$

here, $P(x,z)$ represent the material properties, P_c and P_m are the material properties of ceramic and metal, respectively, and α is the porosity coefficient. $\frac{\alpha}{2}(P_c + P_m)$ represents the porosity effect and $\left(1 - \frac{2|z|}{h}\right)$ introduces a linear gradient in porosity in the vertical direction, resulting in areas with different pore densities.

2.3 Displacement field and non-zero stresses and strains

Specific assumptions are employed while choosing displacement fields for HSDT. The displacements in both axial and transverse directions can be classified into bending and shear components. After deformation, the dimensions of the beam remain planar and orthogonal to the deformed axis. The transverse shear strain is considered uniform across the thickness, and it is assumed that shear deformation is independent of bending deformation. The beam is seen as being made of elastic material and conforms to Hooke's law. The shear component of axial displacement induces oscillations in shear strain at higher orders, hence producing shear stress over the entire depth of the beam. The intensity of this shear stress is insignificant on the upper and lower surfaces.

The displacement field equations that satisfy the kinematic assumptions of HSDT that include compatibility, equilibrium and adhere to the constitutive relationships of the beam material are presented in Eqs. (5)-(6) (Karamanli 2018).

$$U(x,z) = u_0(x) + z\emptyset(x) - f(z)\left(\emptyset(x) + \frac{\partial w_0}{\partial x}(x)\right) \tag{5}$$

$$W(x,z) = w_0(x) \tag{6}$$

here, $U(x,z)$ and $W(x,z)$ are the longitudinal and transverse displacements, respectively. $u_0(x)$ is the axial displacement of the beam at mid-point (z=0), $\emptyset(x)$ is the rotation of the neutral axis, $f(z)$ is the shear shape function, $f(z) = \frac{4z^3}{3h^2}$ (Karamanli 2018). The cubic shear shape function guarantees an accurate depiction of the non-linear distribution of transverse shear stresses across the thickness of the beam. $\frac{\partial w_0}{\partial x}$ is the bending slope, $w_0(x)$ is the transverse displacement at mid-point. $f(z)\left(\emptyset(x) + \frac{\partial w_0}{\partial x}(x)\right)$ accounts for the transverse shear deformation effect and $z\emptyset(x)$ captures the rotation of the cross section of the beam due to bending.

The normal strain (ε_x) and axial shear strain (γ_{xz}), along with normal stress (σ_x) and shear stress (τ_{xz}) are given Eqs. (7)-(10) (Chintalapudi *et al.* 2024).

$$\varepsilon_x = \frac{\partial U}{\partial x} = \frac{\partial u_0}{\partial x} - z\frac{\partial^2 w_0}{\partial x^2} + f(z)\left(\frac{\partial \emptyset}{\partial x} + \frac{\partial^2 w_0}{\partial x^2}\right) \tag{7}$$

$$\gamma_{xz} = f'\left[\emptyset(x) + \frac{\partial w_0}{\partial x}\right] \tag{8}$$

$$\sigma_x = E(x)\varepsilon_x \tag{9}$$

$$\tau_{xz} = \frac{E(x)}{2(1+\mu)}\gamma_{xz} \tag{10}$$

here, $-z\frac{\partial^2 w_0}{\partial x^2}$ accounts for the bending induced strain, $E(x)$ is the Young’s modulus and μ is the Poisson’s ratio.

The spatial variation of $E(x)$ reflects the effect of material gradation along the length and thickness of the beam. This is essential for accurately modeling the behavior of FGPB, where material properties transition continuously between metal and ceramic phases. The equations provide a comprehensive representation of the coupled effects of axial, bending, and shear deformations on the structural behavior of the beam by including bending and shear deformation terms in ε_x and γ_{xz}.

2.4 Formulation of governing equations

The strain energy equation quantifies the elastic energy retained in a structure because of deformation from applied loads, accounting for both axial and shear deformations in the structural behavior. The total strain energy (δU) for the FGPB is given in Eq. (11) (Gao *et al.* 2024).

$$\delta U = \frac{1}{2}\int_0^L \int_{-\frac{h}{2}}^{+\frac{h}{2}} (\sigma_x \varepsilon_x + \tau_{xz}\gamma_{xz}) dzdx \tag{11}$$

The axial strain energy ($\sigma_x \varepsilon_x$), represents the energy stored due to normal stress in the longitudinal direction due to the axial and bending deformations. The shear strain energy, $\tau_{xz}\gamma_{xz}$, represents the energy stored due to the transverse shear stress that arises from the combined effects of shear deformation and rotation. The strain energy equation is a key component in deriving the governing equations for structural stability (buckling) that allows for a unified treatment of both phenomena by incorporating axial and shear effects. By incorporating the strain energy into the total potential energy of the system, critical buckling loads can be determined using the principle of minimum potential energy. Substituting Eqs. (7)-(10) into Eq. (11), the strain energy could be deduced as shown in Eqs. (12)-(13).

$$\partial U = \int_0^L \int_A \left\{\sigma_x \left[\frac{du_o}{dx} + 2\frac{d\emptyset}{dx} - f(z)\left(\frac{d\emptyset}{dx} + \frac{\partial^2 w_0}{\partial x^2}\right)\right] + \sigma_{xz}\left[\left(\frac{\partial w_0}{\partial x} + \emptyset - \frac{4z^2}{3h^2}\left(\emptyset + \frac{\partial w_0}{\partial x}\right)\right)\right]\right\} dAdx \tag{12}$$

$$\partial U = \int_0^L \int_A \left\{\sigma_x \left[\frac{du_o}{dx} + 2\frac{d\emptyset}{dx} - \frac{4z^2}{3h^2}\frac{d\emptyset}{dx} - \frac{4z^2}{3h^2}\frac{\partial^2 w_0}{\partial x^2}\right] + \sigma_{xz}\left[\left(\frac{\partial w_0}{\partial x} + \emptyset - \frac{4z^2}{h^2}\emptyset - \frac{4z^2}{h^2}\frac{\partial w_0}{\partial x}\right)\right]\right\} dAdx \tag{13}$$

If, M_x, Q_x are the bending moment and the shear force. P_x and R_x are the higher order stress resultants, Eq. (13) can be modified into Eq. (14)

$$M_x = \int_A z\sigma_x dA,\ P_x = \int_A z^3\sigma_x dA,\ N_x = \int_A \sigma_x dA$$

$$R_x = \int_A z^2\sigma_{xz} dA,\ Q_x = \int_A \sigma_{xz} dA \tag{14}$$

$$\partial U = \int_0^L \left[N_x\frac{du_0}{dx} + M_x\frac{d\emptyset}{dx} - \frac{4}{3h^2}P_x\frac{d\emptyset}{dx} - \frac{4}{3h^2}P_x\frac{d^2 w_0}{dx^2} + Q_x\frac{dw_0}{dx} + Q_x\emptyset - \frac{4}{h^2}R_x\emptyset - \frac{4}{h^2}R_x\frac{dw_0}{dx}\right]dx$$

Potential work is essential for analyzing the relationship between external forces and structural deformation. The work performed by transverse loads on beams directly affects the total potential energy of the beam, hence determining its stability and deformation characteristics. The prospective impact of the transverse load is significant for FGPB, since variations in material gradation and porosity distributions increase the complexity. The potential work (∂V), of a transverse load ($q(x)$) acting on the FGPB is given in Eq. (15) (Bridjesh *et al.* 2023).

$$\partial V = -\int_0^L q(x) w_0 dx \tag{15}$$

Eq. (15) accommodates diverse transverse load distributions, rendering it relevant to various practical applications, including uniform loads, point loads, or linearly variable loads.

The total potential energy gives an account of energy status of the beam, which includes the strain energy that arises within the beam and the potential work that is external to the beam. Buckling loads are some of the critical stability conditions that can be analyzed through the principle of the minimum potential energy. The total potential energy (Π) of the FGPB is given in Eq. (16) (Jiao *et al.* 2024).

$$\Pi = \partial U + \partial V \tag{16}$$

Substituting Eqs. (14)-(15) into Eq. (16),

$$\begin{aligned}\Pi &= \left[N_x u_0 + \left(M_x - \frac{4}{3h^2}P_x\right)\emptyset + (Q_x + R_x)w_0\right]_0^L \\ &+ \int_0^L \left[\frac{dN_x}{dx}u_0 + \left(\frac{4}{3h^2}\frac{dP_x}{dx} - \frac{dM_x}{dx} + Q_x - \frac{4}{3h^2}R_x\right)\emptyset - \left(q + \frac{dQ_x}{dx} + \frac{dR_x}{dx}\right)w_0\right]dx = 0\end{aligned} \tag{17}$$

Specify,

$$\begin{Bmatrix} u_0 \\ w_0 \\ \emptyset \end{Bmatrix} \quad OR \quad \begin{Bmatrix} N_x \\ Q_x + R_x \\ M_x - \dfrac{4}{3h^2}P_x \end{Bmatrix} \tag{18}$$

The equilibrium equations can be expressed as Eqs. (19)-(21).

$$\frac{dN_x}{dx} = 0 \tag{19}$$

$$\frac{4}{3h^2}\frac{dP_x}{dx} - \frac{dM_x}{dx} + Q_x - \frac{4}{3h^2}R_x = 0 \tag{20}$$

$$q + \frac{dQ_x}{dx} + \frac{dR_x}{dx} = 0 \tag{21}$$

Eqs. (19)-(21) represents the equilibrium conditions derived from minimum potential energy that characterizes the stability of the FGPB. These equations summarize the mechanical interactions affected by material gradation, porosity distributions, and the imposed boundary conditions. The governing equations are solved utilizing KKT conditions.

The buckling analysis of FGPB is governed by intricate equations that include complex constraints from material gradation, porosity distribution, geometrical considerations and boundary conditions. KKT conditions offer a framework for including any of these constraints into the solution process to ensure a correct and optimal evaluation of critical buckling loads. A primary feature of the KKT method is its capacity to address nonlinear governing equations associated with HSDT where the KKT conditions significantly reduce the problem to a system of algebraic equations to be solved.

2.5 Karush-Kuhn-Tucker conditions

The KKT conditions are fundamental circumstances for optimality in nonlinear improvement issues with disparity and correspondence limitations. They are an augmentation of the Lagrange

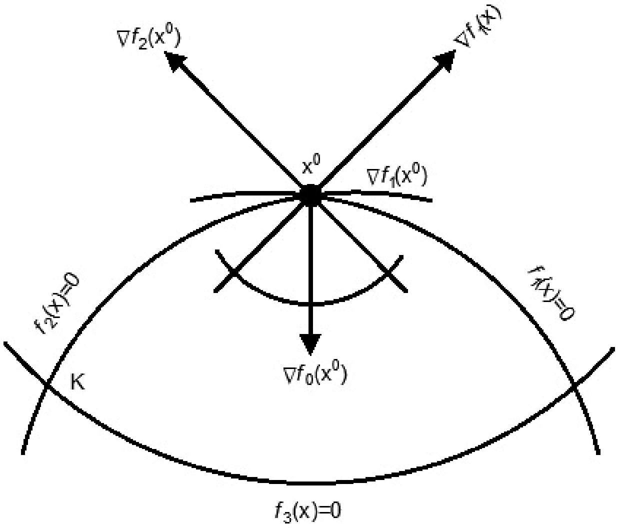

Fig. 2 Conditions that satisfy the KKT method

multiplier strategy for compulsory streamlining problems. The KKT conditions are a collection of conditions that should be fulfilled at an optimal value, Li and Hu (2024).

Minimize f(x)
subject to gi(x)≤0, i=1,2, …, m
hj(x)=0, j=1,2, …, p
$\nabla f(x) + \sum_{i=1}^{m} \lambda_i \nabla$ gi(x)+ $\sum_{i=1}^{p} v_i \nabla$ hi(x)=0

Consider the second term f(x)= $\sum_{i=1}^{m} \lambda_i \nabla$ gi(x)

These conditions guarantee that the optimal value fulfills both the imperatives and the optimality models. They are important conditions, intending that assuming an answer is optimal, it should fulfill these conditions. In any case, they are not generally adequate for optimality. Now and again, extra conditions or calculations might be expected to check optimality.

Assume that $f_k(x)$ $(k = 0, 1, 2, \ \dots, m)$ are all differentiable if the function $f_0(x)$ attains at point x^0 a local minimum subject to the set $K = \left\{\frac{x}{f_i(x)} \leq 0(i = 1, 2, 3, \dots, m)\right\}$ then there exist a vector of Lagrange multiplier U^0 such that the following conditions are satisfied, as illustrated in Fig. 2.

$$\frac{\partial f_0(x^0)}{\partial x_j} + \sum_{i=1}^{m} U_i^0 \frac{\partial f_0(x^0)}{\partial x_j} = 0 \ (j = 1, 2, 3, \dots \dots, n)$$

$$f_i(x^0) \leq 0 \ (i = 1, 2, 3, \dots . m)$$

$$u_i^0 f_i(x^0) = 0 \ (i = 1, 2, 3, \dots . , m)$$

$$u_i^0 \ \geq 0 \ (i = 1, 2, 3, \dots . m)$$

These conditions are necessary conditions for a local minimum of problems, for maximization problems, the non-negativity condition $U^0 \leq 0$, are called the KKT condition (Feng *et al*. 2022)

$$L(x, z, u) = \ f_0(x) + \sum_{i=1}^{m} u_i(f_i(x) + z_i^2)$$

The necessary conditions for its local minimum are,

$$\frac{\partial L}{\partial x_j} = \frac{\partial f_0(x^0)}{\partial x_j} + \sum_{i=1}^{m} u_i^0 \frac{\partial [f_i(x^0) + (z_i^0)^2]}{\partial x_j} = 0$$

$\frac{\partial L}{\partial z_i} = 2u_i^0 z_i^0 = 0 \ \ (j = 1, 2, 3, \ldots.n)$

$\frac{\partial L}{\partial u_i} = f_i(x^0) + (z_i^0)^2 = 0 \ \ (i = 1, 2, 3, \ldots m)$

$\frac{\partial f_0[x^0(b)]}{\partial b_i} = -u_i^0 \ \ (i = 1, 2, 3, \ldots.m)$

Without slack variables, the mathematical problem,

$L(x, u) = f_0(x) + \sum_{i=1}^{m} u_i f_i(x)$

The KKT condition can be rewritten as,

$\frac{\partial L(x^0, u^0)}{\partial x_j} = 0 \ \ (j = 1, 2, 3, \ldots..n)$

$\frac{\partial L(x^0, u^0)}{\partial u_i} \leq 0 \ \ (i = 1, 2, 3, \ldots..m)$

$u_i^0 \frac{\partial L(x^0, u^0)}{\partial u_i} = 0 \ \ (i = 1, 2, 3, \ldots..m)$

$u_i^0 \geq 0 \ (i = 1, 2, 3, \ldots m)$

If the multiplier u_i is positive, then the corresponding ith constraint is the boundary solution. When the function $u_0(x, \mathrm{z})$, $w_0(x, z)$, and $\emptyset_0(x, \mathrm{z})$ are expressed as generalised co-ordinates, it can be represented as Lagrange equations, as shown in Eqs. (22)-(24).

$$u_0(x, \mathrm{z}) = \sum_{i=1}^{m} f_i(x^0)\theta_i e^{i\lambda z} \tag{22}$$

$$w_0(x, z) = \sum_{i=1}^{m} f_i(x^0)\varphi_i e^{i\lambda z} \tag{23}$$

$$\emptyset_0(x, z) = \sum_{i=1}^{m} f_i(x^0)\psi_i e^{i\lambda z} \tag{24}$$

Simillarly for f(x)= $\sum_{i=1}^{p} v_i \nabla$ hi(x)

If the multiplier $u_i$is positive, then the corresponding ith constraint is the boundary solution. When the function $u_0(x, \mathrm{z})$, $w_0(x, z)$, and $\emptyset_0(x, \mathrm{z})$ are expressed as generalised co-ordinates, it can be represented as Lagrange equations, as shown in Eqs. (25)-(27).

$$u'_0(x, \mathrm{z}) = \sum_{i=1}^{p} f_i(x^0)\theta_i e^{i\lambda z} \tag{25}$$

$$w'_0(x, z) = \sum_{i=1}^{p} f_i(x^0)\varphi_i e^{i\lambda z} \tag{26}$$

$$\emptyset'_0(x, z) = \sum_{i=1}^{p} f_i(x^0)\psi_i e^{i\lambda z} \tag{27}$$

where, θ_i, φ_i, and ψ_i are the three different boundary conditions and λ is the scalar. The boundary conditions based on the KKT conditions are shown in Table 1.

Table 1 Input parameter minimum and maximum values

Boundary condition	$x = 0$	$x = L$
SS	$u = 0,\ w \leq 0$	$w = 0$
CS	$u = 0,\ w \leq 0,\ \emptyset = 0,\ w' \leq 0$	$u = 0$
CC	$u = 0,\ w \leq 0,\ \emptyset = 0,\ w' \leq 0$	$u = 0,\ w \leq 0,\ \emptyset = 0,\ w' \leq 0$
CF	$u = 0,\ w = 0,\ \emptyset = 0,\ w' = 0$	--

$$\begin{gathered}
\frac{\partial^2 \pi}{\partial M_j^2} = 0,\ \frac{\partial^2 \pi}{\partial N_j^2} = 0,\ \frac{\partial^2 \pi}{\partial P_j^2} = 0 \\
\left\{\begin{bmatrix} F_{11} & F_{12} & F_{13} \\ F_{21} & F_{22} & F_{23} \\ F_{31} & F_{32} & F_{33} \end{bmatrix} - \lambda^2 \begin{bmatrix} 0 & 0 & 0 \\ 0 & R_{22} & 0 \\ 0 & 0 & 0 \end{bmatrix}\right\} \begin{bmatrix} M \\ N \\ P \end{bmatrix} = \begin{bmatrix} 0 \\ 0 \\ 0 \end{bmatrix} \\
\left\{\begin{bmatrix} F_{11} & F_{12} & F_{13} \\ F_{21} & F_{22} & F_{23} \\ F_{31} & F_{32} & F_{33} \end{bmatrix} - \begin{bmatrix} 0 & 0 & 0 \\ 0 & \lambda^2 R_{22} & 0 \\ 0 & 0 & 0 \end{bmatrix}\right\} \begin{bmatrix} M \\ N \\ P \end{bmatrix} = \begin{bmatrix} 0 \\ 0 \\ 0 \end{bmatrix} \\
F_{11}(i,j) = M \int_0^L e^{\lambda x(x+1)}\, \theta_{i,x}, \theta_{j,x} dx \\
F_{12}(i,j) = F_{21}(i,j) = P \int_0^L e^{\lambda x(x+1)}\, \theta_{i,x}, \theta_{j,x} dx \\
F_{13}(i,j) = F_{31}(i,j) = (N - \alpha M) \int_0^L e^{\lambda(x+1)}\, \theta_{i,x}, \varphi_{i,x} dx \\
F_{22}(i,j) = \alpha^2 [F_{12}(i,j)][F_{13}(i,j)] \\
F_{23}(i,j) = F_{32}(i,j) = (\beta^2 - \alpha F)[F_{22}(i,j)] \\
F_{33}(i,j) = \lambda^2 R_{22} \int_0^L e^{\lambda x(x+1)}\, \theta_i, \theta_i dx \\
R_{11} = R_{12} = R_{13} = R_{21} = R_{23} = R_{31} = R_{32} = R_{33} = 0 \\
R_{22}(i,j) = (\alpha^2 M - \beta N)[F_{33}(i,j)], \text{ where, } i,j = 1, 2, 3, \ldots \ldots n
\end{gathered} \tag{28}$$

3. Validation of mathematical formulation

To evaluate the applicability of the proposed methodology, a case has been made to analyze the impact of gradient indexes, aspect ratios and porosity parameters on the buckling behavior of FGPB. The combined effect of material gradation and structural parameters are focused considering alumina as ceramic and aluminum as metal. The physical properties of alumina and aluminum are shown below (Bridjesh *et al.* 2023):

Aluminum: E_m=70 GPa, μ_m=0.3, and

Alumina: E_c=380 GPa, μ_c=0.3

here, E_m and E_c are Young's modulus of metal and ceramic. μ_m and μ_c are Poisson's ratio of metal and ceramic, respectively.

The dimensionless critical buckling load ($\overline{N}_{cr}$) is evaluated using Eq. (29).

$$\overline{N}_{cr} = \frac{12 N_{cr} L^2}{E(x,z) b h^3} \tag{29}$$

Table 2 Verification and convergence analyses of the $\overline{N}_{cr}$ under various boundary conditions and aspect ratio

Boundary condition	L/h	Beam theory						
		Bridjesh *et al.* 2023	Karamanli 2018	Present				
				2 terms	4 terms	6 terms	8 terms	10 terms
SS	5	50.163	48.596	52.127	51.987	51.342	51.342	51.342
	20	57.813	53.236	61.753	60.135	59.684	59.684	59.684
CS	5	-	105.174	104.751	103.874	102.318	102.318	102.318
	20	-	108.051	115.621	114.876	113.282	113.282	113.282
CC	5	154.351	152.147	214.941	209.744	153.295	153.295	153.295
	20	205.851	208.951	187.524	181.645	170.418	170.418	170.418
CF	5	13.327	13.059	14.941	14.352	12.569	12.569	12.569
	20	13.785	13.373	14.257	13.894	13.132	13.132	13.132

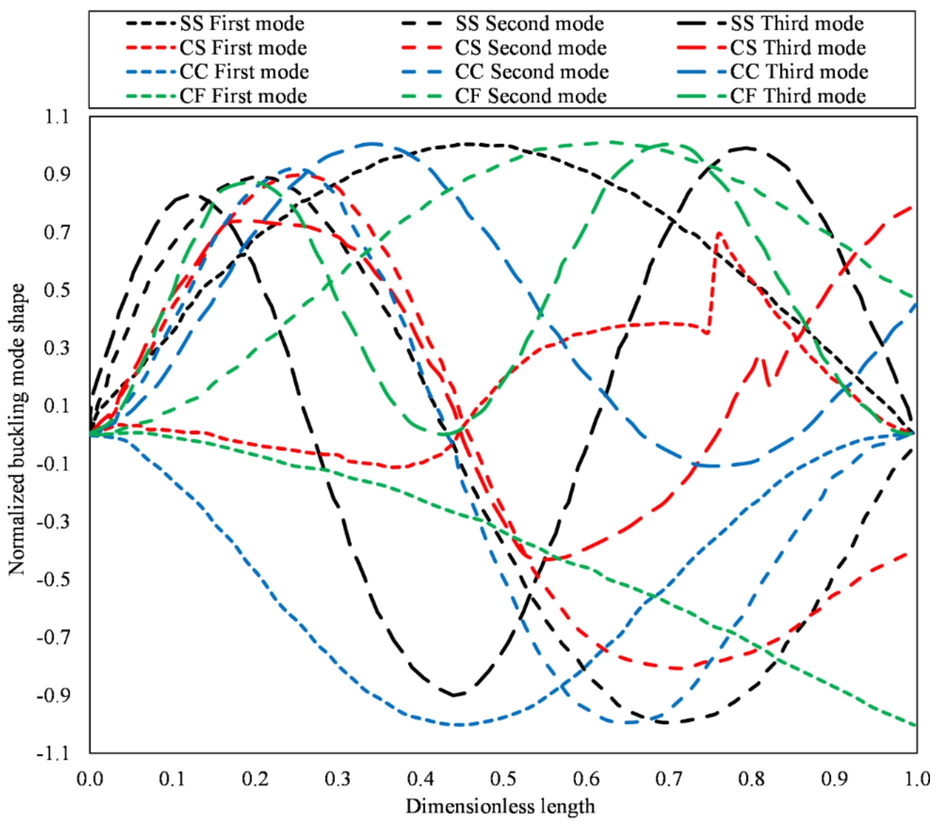

Fig. 3 The normalized buckling mode shapes of FGPB under SS, CS, CC, and CF boundary conditions

here, N_{cr} is the critical buckling load and $E(x,z)$ is the effective Young's modulus of the FGPB.

To ensure that the results are consistent, and the findings can be applied at a larger scale, the dimensionless formulation allows for comparison of data from different research, material properties and structural geometries. The analysis is performed for four distinct boundary conditions such as, SS, CS, CF, and CC. A convergence analysis is performed using a homogeneous beam as a baseline to verify the accuracy of the proposed method. Displacement functions with varying numbers of terms are employed to estimate the stability of the results to ensure numerical robustness. The results are compared to established data from prior studies (Bridjesh *et al.* 2023, Karamanli 2018), and the findings are shown in Table 2.

The results from the present methodology converge rapidly as the number of terms in the displacement function increases. For all boundary conditions and aspect ratios, the results stabilize beyond six terms that indicate numerical robustness. For example, under SS boundary conditions, the $\bar{N}_{cr}$ stabilizes at 51.342 and 59.684 with $L/_h$=5 and 20, respectively. The present results are in good agreement with those reported by (Bridjesh *et al.* 2023) and Karamanli (2018), with minor deviations attributed to differences in modeling assumptions and methodologies. In CF configuration, at $L/_h$=5, the present results (13.132) align well with (Bridjesh *et al.* 2023) (13.327) and Karamanli (2018) (13.059). The consistency of the results at further terms in the displacement function confirms the numerical stability and accuracy of the presented method applicable for detailed analysis of the material gradation and porosity field, Turan and Adhiyaman (2024). The percentage error (E_0) in the estimation of $\bar{N}_{cr}$ is done using Eq. (30). For 2nd and 6th terms of SS, CS, CC, and CF boundary conditions, the error is found to be 1.51, 3.35, 2.32, 2.02, 28.68, 9.12, 15.88, and 7.89%, respectively.

$$E_0 = \left|\frac{\bar{P}_N - \bar{P}_{N-1}}{\bar{P}_{N-1}}\right| x\,100 \tag{30}$$

here, E_0 is the % error, $\bar{P}_N$ is the specified term, $\bar{P}_{N-1}$ is the desired term.

4. Results and discussion

4.1 Buckling mode shapes

Buckling modes are of enormous importance in determining the stability and the load-carrying capacity of structural members. All the modes depict a different deformation pattern and the associated critical buckling load. They aid in determining the values at which point the structure moves from a stable to an unstable state. The variations in dimensionless length and normalized critical buckling loads for the FGPB under SS, CS, CC, and CF boundary conditions under the first, second, and third buckling modes are shown in Fig. 3.

Under SS boundary conditions, the normalized buckling load increases rapidly as the dimensionless length increases. The growth rate is nonlinear, with a steep rise at smaller lengths and gradually tapering off as the length increases. For short beams, where dimensionless length < 0.1, the buckling load is significantly smaller which indicates high sensitivity to changes in beam length. The critical buckling loads for the second mode are higher than those of the first mode for the same dimensionless length. The buckling load increases more slowly in the second mode that exhibits a slightly flatter curve compared to the first mode. The second mode is associated with higher stability due to the presence of an additional deformation node in the beam. The critical buckling load increases even more slowly compared to the first and second modes. This is due to the greater complexity of the deformation shape and additional nodes along the length of the beam. For small dimensionless lengths (dimensionless length<0.3), it is observed that the buckling load closely aligns with the second mode but diverges significantly as the length increases. The higher modes exhibit more deformation nodes that distribute the compressive stress more efficiently which increases the critical buckling load.

Under CS boundary conditions, the normalized buckling load initially increases with dimensionless length up to a critical value (0.15), beyond which it begins to decrease. This behavior highlights a region of maximum stability at intermediate lengths. The normalized buckling load becomes negative at higher dimensionless lengths (>0.15) that correspond to unstable configurations or loss of critical buckling strength. The critical buckling strength has a highly sensitive dependency of the length, for short lengths positive and stable buckling loads are observed for beams, whereas for extended lengths instabilities are observed. The second mode shows a distinct increase in normalized buckling load with increasing dimensionless length. The second mode exhibits higher normalized buckling loads for the same dimensionless length that reflect greater stability. Dimensionless lengths in the range of 0.2-0.3 offer the highest critical buckling loads that suggest an optimal length range for enhanced performance under CS boundary conditions. The third buckling mode exhibits a similar pattern to the second mode but with higher critical buckling loads at shorter lengths. The third mode exhibits further deformation nodes and is efficient in distributing compressive stress.

Under CC boundary conditions, the normalized buckling load decreases steadily and reaches a minimum around a dimensionless length of 0.5. Beyond this, the load gradually increases and stabilizes near zero for larger lengths. For lengths greater than 0.1, the normalized buckling load becomes negative that indicates a regime where the critical buckling resistance reduces due to higher deformation. The second mode demonstrates a consistent increase in normalized buckling load as the dimensionless length increases. The peak critical buckling load occurs at a mid-range length that suggests an optimal design length for achieving maximum stability in this mode. The second mode reflects greater resistance to buckling compared to the first mode which is evidenced by its higher normalized buckling loads for equivalent lengths. The third mode exhibits the highest normalized buckling loads which increase sharply with dimensionless length. This mode shows the greatest critical buckling resistance across all lengths which is attributed to the additional deformation nodes that efficiently distribute compressive forces.

Under CF boundary conditions, the normalized buckling load in first mode starts near zero for very short beams i.e. dimensionless length<0.02 and decreases gradually. The presence of negative loads for longer beams indicates instability or reduced resistance to buckling under these boundary conditions. The normalized buckling load exhibits a consistent rise with increasing dimensionless length in the second mode. The maximum normalized buckling load is achieved at mid-range lengths that emphasize the significance of optimizing the length of beam for stability in this mode. The third mode shows the highest normalized buckling loads that increase sharply with dimensionless length. This mode demonstrates superior resistance to buckling due to its higher load-carrying capacity and additional deformation nodes that improve the distribution of stresses.

4.2 Effect of gradient index on dimensionless critical buckling

The $\overline{N}_{cr}$ is a key parameter in structural stability analysis for beams and plates under compressive loads. This is because the representation of the buckling load in a normalized and non-dimensional form presents major benefits when comparing the performance of the structures in terms of their configurations and environmental conditions.

The effect of gradient indexes (P_x and P_z) on the $\overline{N}_{cr}$ at various aspect ratios under SS

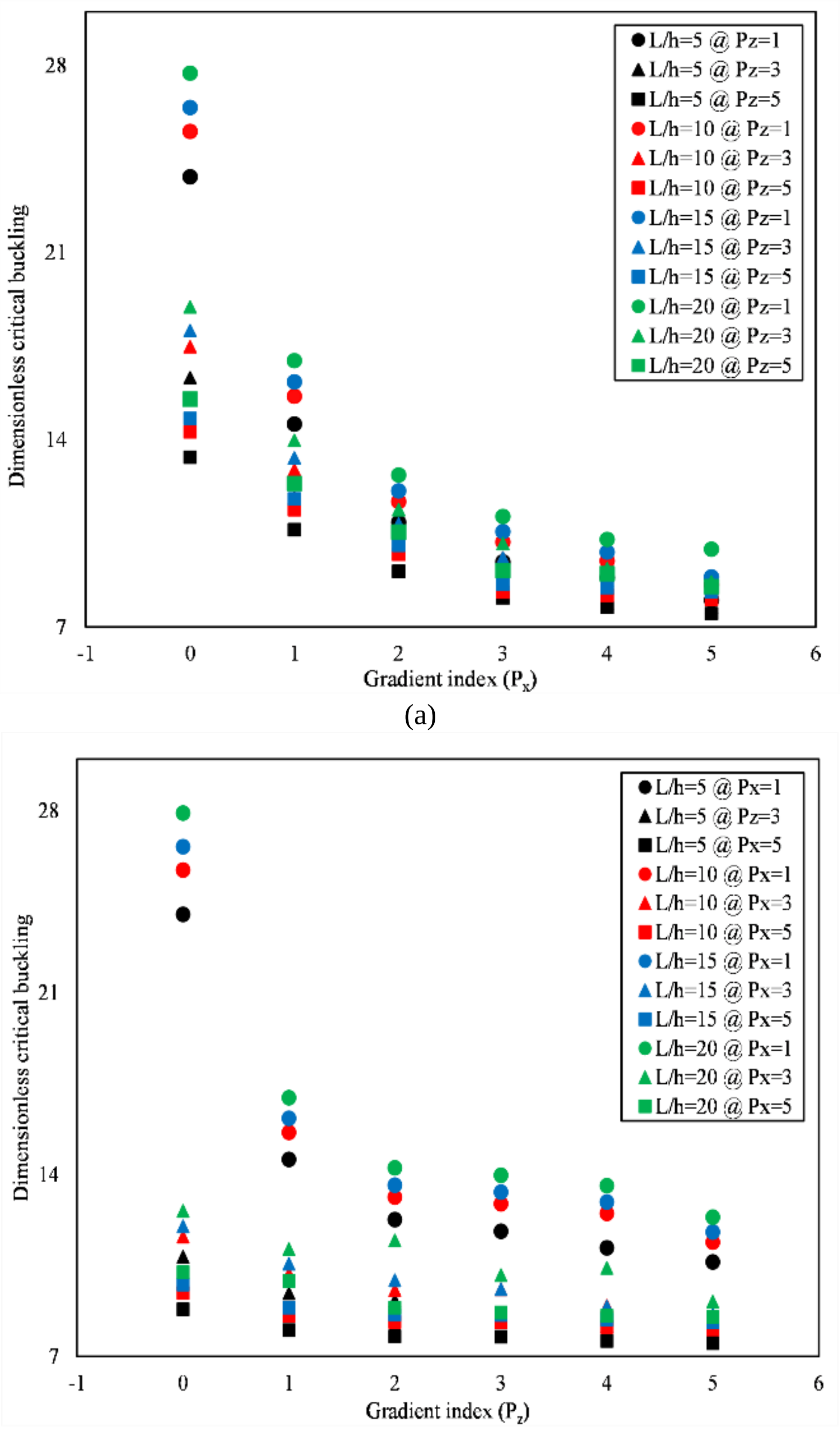

(a)

(b)

Fig. 4 The effect of gradient indexes, (a) P_x, and (b) P_z on the $\overline{N}_{cr}$ at various aspect ratios under SS boundary conditions

Table 3 The $\bar{N}_{cr}$ of the SS FGPB at various P_x, P_z and $^{L}/_{h}$

Gradient index	Px	$^{L}/_{h}$=5						$^{L}/_{h}$=10					
		0	1	2	3	4	5	0	1	2	3	4	5
Pz	0	51.342	24.016	14.668	10.838	9.946	8.811	54.992	25.724	15.710	11.609	10.654	9.437
	1	23.835	14.586	10.911	9.434	8.844	8.009	25.530	15.623	11.687	10.176	9.472	8.578
	2	17.264	12.263	9.921	9.159	8.463	7.770	18.492	13.134	10.626	9.560	9.065	8.322
	3	16.316	11.821	9.798	8.569	7.896	7.752	17.476	12.876	10.495	9.587	8.457	8.303
	4	14.729	11.175	9.616	8.150	7.878	7.588	15.777	12.505	10.300	8.949	8.438	8.128
	5	13.351	10.637	9.078	8.093	7.736	7.504	14.301	11.393	9.723	8.311	8.186	8.038
Gradient index	Px	$^{L}/_{h}$=15						$^{L}/_{h}$=20					
		0	1	2	3	4	5	0	1	2	3	4	5
Pz	0	56.903	26.618	16.256	12.012	11.024	9.765	59.684	27.919	17.051	12.599	11.563	10.242
	1	26.417	16.166	12.093	10.564	9.802	8.877	27.708	16.956	12.684	11.129	10.281	9.910
	2	19.135	13.591	10.995	9.927	9.380	8.612	20.070	14.255	11.533	11.461	9.838	8.877
	3	18.083	13.324	10.860	9.582	8.751	8.592	18.967	13.975	11.390	10.124	9.179	8.692
	4	16.325	12.939	10.658	8.920	8.731	8.410	17.123	13.572	11.179	10.405	9.158	8.560
	5	14.797	11.789	10.061	8.611	8.472	8.317	15.521	12.365	10.553	9.106	8.993	8.512

boundary conditions is illustrated in Figs. 4(a) and (b). With an increase in P_x, the $\bar{N}_{cr}$ decreases for all P_z and $^{L}/_{h}$ values. This trend indicates that a higher longitudinal gradient weakens the stability of the beam under buckling loads. Increasing P_x reduces the stiffness in the longitudinal direction by shifting the material composition from ceramic (higher stiffness) toward metal (lower stiffness). This has the effect of reducing the ability to support axial compressive loads and therefore critical buckling loads are achieved at lower levels (Reddy *et al.* 2024). Thus, the $\bar{N}_{cr}$ reduces from 51.342 at P_x=0 to 8.811 at P_x=5 at $^{L}/_{h}$=5 and P_z=0 which clearly demonstrates the effect of longitudinal material gradation reducing the stability index of the structure. In the buckling analysis of FGPB adapting FEM by Turan and Adhiyama (2024), under similar conditions, the $\bar{N}_{cr}$ was found to be 45.7185 and 6.6824. This difference could be attributed to the discretization and numerical approximations considered in FEM.

The $\bar{N}_{cr}$ reduces as P_z increases at a specific P_x and $^{L}/_{h}$. However, this reduction is not as steep as with the case of P_x. Dependent on Pz, the transverse stiffness alters the distribution of material through the span of the beam. With an increase in P_z, the beam has minimal capacity to bear bending and shear stress which are important in compressive stability. The effect of P_z is considerably lower than that of P_x since material continuity transverse to the beam width basically deals with bending stiffness rather than axial stiffness (Derikvand *et al.* 2023). For instance, at $^{L}/_{h}$=5 and P_x=0 the $\bar{N}_{cr}$ is reduced from 51.342 (P_z=0) to 13.351 (P_z=5) implying reduced influence of P_z compared to P_x. Similar results were obtained by Nathi (2022) in the buckling analysis of FGB (48.5967, 15.6443).

The aspect ratio defines the slenderness of the beam. The aspect ratio is a dominant factor in buckling behavior and higher ratios significantly reducing stability. This highlights the importance of considering beam geometry alongside material gradation. The $\bar{N}_{cr}$ increases significantly as

Table 4 The $\bar{N}_{cr}$ of the CS FGPB at various P_x, P_z and L/h

Gradient index	x	L/h=5						L/h=10					
		0	1	2	3	4	5	0	1	2	3	4	5
Pz		102.318	43.856	28.748	21.923	20.873	19.508	109.586	46.971	30.790	23.480	22.355	20.893
		48.953	28.411	21.977	20.596	19.036	17.154	52.430	30.429	23.538	22.059	20.388	18.372
		35.276	23.860	19.785	19.054	16.976	16.325	37.782	25.554	21.190	20.408	18.182	17.485
		33.361	22.473	19.216	18.316	16.751	16.198	35.730	24.069	20.581	19.616	17.941	17.349
		29.912	20.938	18.360	17.945	16.692	15.866	32.036	22.426	19.664	19.220	17.878	16.993
		25.821	20.151	17.793	17.321	16.721	15.523	27.655	21.582	19.056	18.551	17.908	16.625
Gradient index	x	L/h=15						L/h=20					
		0	1	2	3	4	5	0	1	2	3	4	5
Pz		111.434	47.754	31.308	23.877	22.735	21.250	113.282	48.537	31.826	24.274	23.114	21.607
		53.317	30.940	23.935	22.430	20.735	18.685	54.205	31.452	24.333	22.802	21.082	18.997
		38.421	25.984	21.548	20.751	18.488	17.782	39.060	26.414	21.905	21.093	18.795	18.078
		36.335	24.471	20.927	19.946	18.246	17.643	36.939	24.874	21.274	20.275	18.551	17.938
		32.578	22.799	19.994	19.544	18.182	17.281	33.120	23.172	20.324	19.869	18.486	17.569
		28.119	21.944	19.377	18.864	18.213	16.907	28.584	22.305	19.698	19.177	18.518	17.189

the aspect ratio increases for all combinations of P_x and P_z (Bridjesh *et al.* 2023). A higher L/h ratio corresponds to a longer and slender beam that is more prone to buckling under compressive forces. The $\bar{N}_{cr}$ of the SS FGPB at various P_x, P_z and L/h is presented as Table 3.

The effect of gradient indexes (P_x and P_z) on the $\bar{N}_{cr}$ at various aspect ratios under CS boundary conditions is illustrated in Figs. 5(a) and (b). The $\bar{N}_{cr}$ reduces as P_x increases for all values of P_z and L/h (Bridjesh *et al.* 2024). The decrease in critical buckling stress underscores the detrimental impact of increased longitudinal material gradation on beam stability. The buckling load decreases markedly between P_x=1 and P_x=5. For example, at L/h=5 and P_z=0, $\bar{N}_{cr}$ is reduced from 43.856, for P_x=1 to 19.508 for P_x=5. This trend is similar across higher aspect ratios as well. At *L*/*h*=20 and P_z=0 it is 21.607 when P_x=5. Whereas, at L/h=20 and P_z=0, P_x=1 it is 48.537. Under similar conditions, Karamanli (2018) got the values 29.5651 and 55.1941 for L/h=5 and 20, respectively. The difference in these values may be attributed to the homogenous beam adapted by Karamanli (2018) and the porous beam being used in this study. Increasing P_x corresponds to a longitudinal material gradient that reduces the overall stiffness of the beam in the axial direction. This transition shifts the composition from stiff ceramic regions to more flexible metal, subsequently decreases the axial stiffness and reduces the resistance to buckling.

Higher L/h ratios indicate longer and thinner beams, and it is well understood that thin and longer beams are more susceptible to fail under axial compression force. This geometrical factor has lower material properties and as the beams get longer the instability increases because of the stiffness. For any value of P_x or P_z, it is observed that the $\bar{N}_{cr}$ drastically decreases with the increase in L/h (Mesbah *et al.* 2023). This decrease is uniform across all gradient indices highlight the primary influence of aspect ratio on beam stability. At P_x=0 and P_z=0, the $\bar{N}_{cr}$

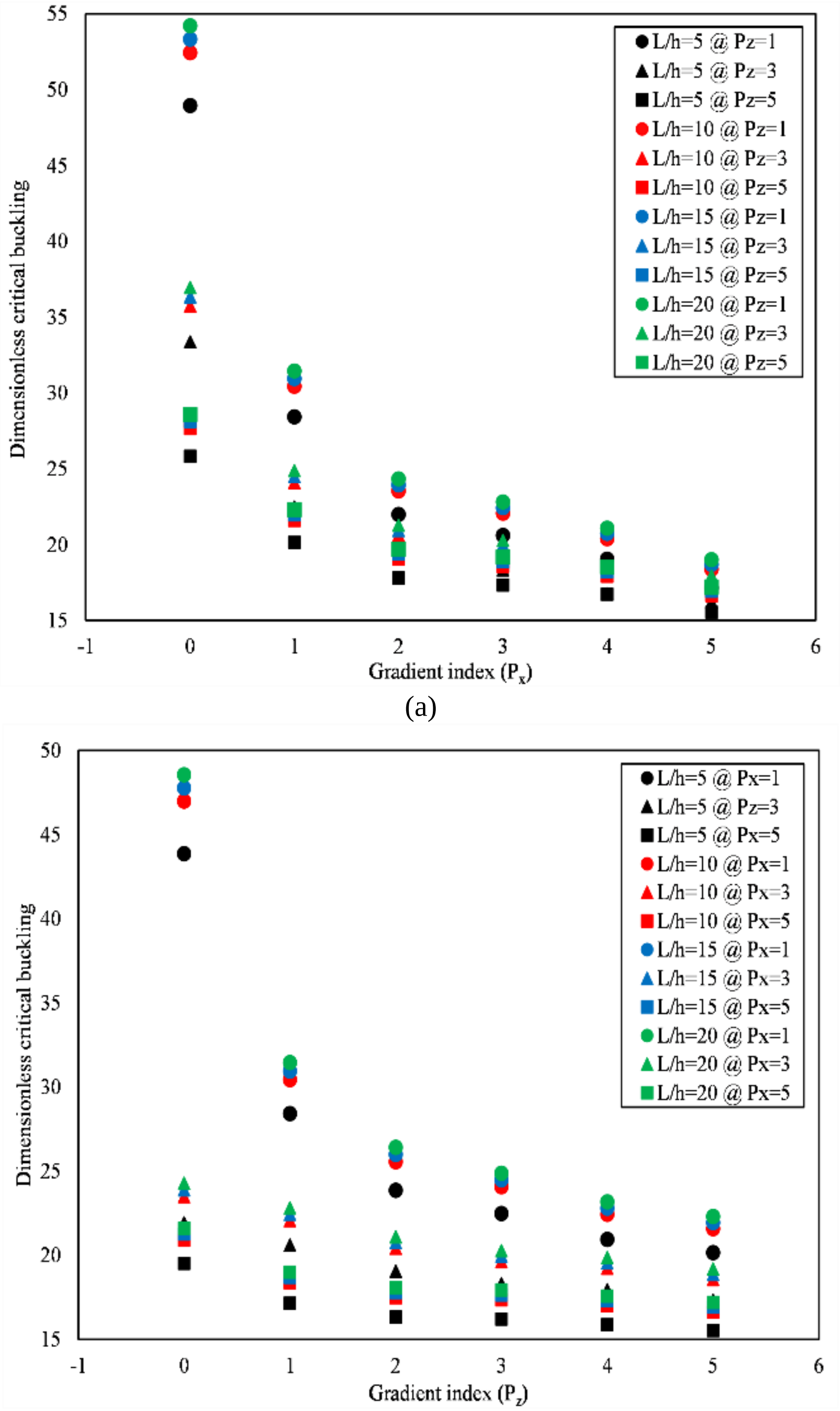

(a)

(b)

Fig. 5 The effect of gradient indexes, (a) P_x, and (b) P_z on the $\overline{N}_{cr}$ at various aspect ratios under CS boundary conditions

Table 5 The $\bar{N}_{cr}$ of the CC FGPB at various P_x, P_z and L/h

Gradient index	x	L/h=5						L/h=10					
		0	1	2	3	4	5	0	1	2	3	4	5
Pz		153.295	63.695	42.828	33.008	31.799	30.205	164.179	68.218	45.869	35.352	34.057	32.349
		74.071	42.236	33.042	30.758	29.229	26.299	79.330	45.234	35.388	32.942	31.304	28.166
		53.288	35.457	29.649	28.250	25.489	24.881	57.072	37.974	31.754	30.256	27.298	26.647
		50.406	32.924	28.634	27.062	25.607	24.645	53.984	35.261	30.667	28.983	27.425	26.395
		45.094	30.202	27.104	26.940	25.507	24.144	48.296	32.347	29.028	28.853	27.318	25.858
		38.290	29.665	26.508	25.949	25.705	23.541	41.009	31.772	28.390	27.792	27.530	25.212
Gradient index	x	L/h=15						L/h=20					
		0	1	2	3	4	5	0	1	2	3	4	5
Pz		167.298	69.514	46.740	36.023	34.704	32.964	170.418	70.810	47.612	36.695	35.351	33.579
		80.837	46.094	36.061	33.568	31.899	28.701	82.344	46.953	36.733	34.194	32.493	29.236
		58.156	38.695	32.358	30.830	27.817	27.153	59.241	39.417	32.961	31.405	28.336	27.660
		55.010	35.931	31.250	29.534	27.946	26.896	56.036	36.601	31.833	30.085	28.467	27.398
		49.214	32.961	29.580	29.401	27.837	26.349	50.131	33.576	30.131	29.949	28.356	26.840
		41.788	32.375	28.929	28.320	28.053	25.691	42.567	32.979	29.469	28.848	28.576	26.170

decreases from 102.318 (L/h=5) to 113.282 (L/h=20). The same tendency is noted for various combinations of P_x and P_z. Despite elevated gradient indexes, specifically P_x=5 and P_z=5, the $\bar{N}_{cr}$ reduces from 19.508 (L/h=5) to 17.189 (L/h=20). The $\bar{N}_{cr}$ of the CS FGPB at various P_x, P_z and L/h is presented as Table 4.

The effect of gradient indexes (P_x and P_z) on the $\bar{N}_{cr}$ at various aspect ratios under CC boundary conditions is illustrated in Figs. 6(a) and (b). Irrespective of P_z and L/h, the $\bar{N}_{cr}$ decreases as P_x increases. This reduction is more pronounced at smaller P_x values but tends to stabilize at higher P_x. The $\bar{N}_{cr}$ from 63.695 (P_x=1) to 30.205 (P_x=5) at L/h=5 and P_z=0 and at L/h=20 and P_z=0, the $\bar{N}_{cr}$ decreases from 70.810 (P_x=1) to 35.579 (P_x=5). Similar findings were observed by Adiyaman and Turan (2024) in the buckling analysis of porous beam using FEM. Increasing P_x represents a stronger longitudinal material gradient that reduces axial stiffness by transitioning the material composition of the beam from stiffer ceramic regions to more flexible metallic regions. This decreased stiffness reduces the resistance to compressive forces which lower the critical buckling load.

For P_z>0, the $\bar{N}_{cr}$ also decreases, though the reduction is less steep compared to P_x. The effect is more noticeable at lower aspect ratios. At L/h=5 and P_x=0, the $\bar{N}_{cr}$ decreases from 153.295 (P_z=0) to 38.290 (P_z=5). At L/h=20 and P_x=0, the $\bar{N}_{cr}$ decreases from 170.418 (P_z=0) to 42.567 (P_z=5). The effect of transverse material gradation is more evident in the bending stiffness than in the axial stiffness (Bridjesh *et al.* 2024). With the increase of P_z, the contribution from more flexible material across the thickness is higher, hence reducing the bending resistance. These reductions in bending stiffness are accompanied by lower $\bar{N}_{cr}$ and this effect is less dominant compared to P_x.

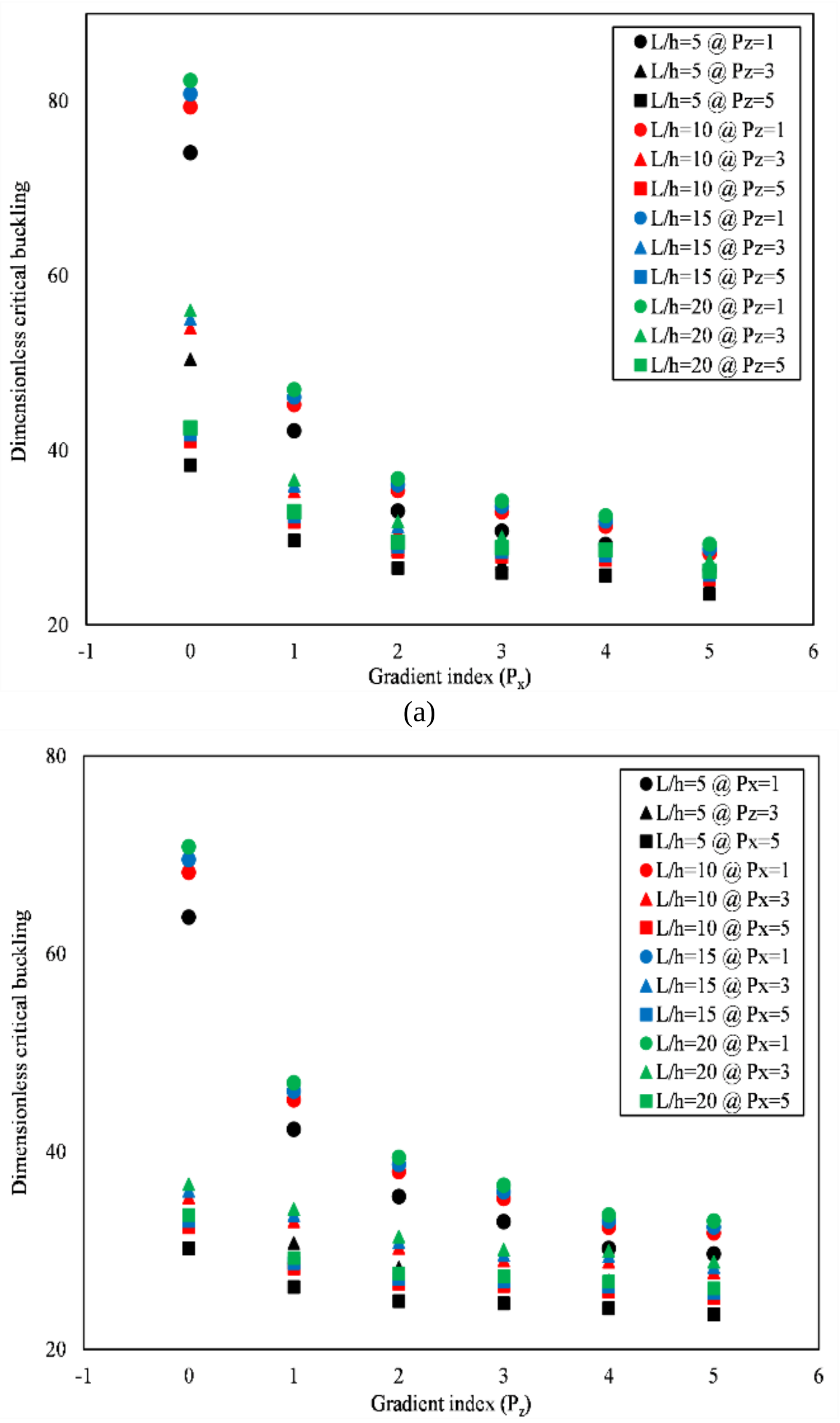

(a)

(b)

Fig. 6 The effect of gradient indexes, (a) P_x, and (b) P_z on the $\overline{N}_{cr}$ at various aspect ratios under CC boundary conditions

Table 6 The $\overline{N}_{cr}$ of the CF FGPB at various P_x, P_z and L/h

Gradient index	Px	L/h=5						L/h=10					
		0	1	2	3	4	5	0	1	2	3	4	5
Pz	0	12.569	3.899	2.509	2.265	2.091	1.848	12.858	3.989	2.567	2.317	2.139	1.891
	1	5.752	2.769	2.137	2.054	1.832	1.777	5.884	2.832	2.186	2.101	1.874	1.817
	2	4.180	2.488	2.036	2.014	1.874	1.755	4.276	2.545	2.083	2.061	1.917	1.796
	3	3.720	2.476	1.988	1.956	1.871	1.752	3.805	2.533	2.033	2.001	1.914	1.793
	4	3.445	2.366	1.956	1.948	1.860	1.733	3.525	2.420	2.001	1.993	1.903	1.773
	5	3.317	2.271	1.942	1.939	1.852	1.731	3.393	2.323	1.987	1.983	1.894	1.771

Gradient index	Px	L/h=15						L/h=20					
		0	1	2	3	4	5	0	1	2	3	4	5
Pz	0	12.995	4.032	2.594	2.342	2.162	1.911	13.132	4.074	2.621	2.366	2.185	1.931
	1	5.947	2.863	2.209	2.124	1.894	1.837	6.010	2.893	2.232	2.146	1.914	1.856
	2	4.321	2.572	2.105	2.083	1.938	1.815	4.367	2.599	2.127	2.105	1.958	1.834
	3	3.846	2.560	2.055	2.022	1.934	1.812	3.886	2.587	2.077	2.044	1.955	1.831
	4	3.562	2.446	2.022	2.014	1.923	1.792	3.600	2.472	2.044	2.035	1.943	1.811
	5	3.429	2.348	2.008	2.004	1.914	1.790	3.466	2.373	2.029	2.025	1.935	1.809

The $\overline{N}_{cr}$ decreases significantly with increasing L/h across all values of P_x and P_z. This trend is consistent and reflects the dominant role of geometry in buckling stability. At P_x=0 and P_z=0, the $\overline{N}_{cr}$ decreases from 153.295 (L/h=5) to 170.418 (L/h=20). Even at higher gradient indexes (P_x=5, P_z=5), the $\overline{N}_{cr}$ decreases from 23.541 (L/h=5) to 26.170 (L/h=20). The higher trends in L/h ratios show more thin beams which are inherently weaker to buckling loads due to reduced stiffness, Nathi (2022). The boundary conditions defining the CC gives the maximal restriction than the geometric effect dominates offers, leading to decrease in the buckling load as slenderness increases. The $\overline{N}_{cr}$ of the CC FGPB at various P_x, P_z and L/h is presented as Table 5.

The effect of gradient indexes (P_x and P_z) on the $\overline{N}_{cr}$ at various aspect ratios under CF boundary conditions is illustrated in Figs. 7(a) and (b). At L/h=5 and P_z=0, $\overline{N}_{cr}$ reduces highly from 12.569, when P_x=0, to 1.848, when P_x=5. The same tendency is noted for higher aspect ratios. At L/h=20 and P_z=0, the $\overline{N}_{cr}$ reduces from 13.132 (P_x=0) to 1.911 (P_x=5). In the buckling analysis of FGB, Nathi (2022) found the values of $\overline{N}_{cr}$ as 13.1567 and 13.474 at L/h=5 and 20, respectively. These findings are in par with the findings of the present study (12.569, 13.132). As P_x increases, the material shifts from rigid ceramics to metals along the length of the beam. This reduces axial stiffness, essential for counteracting compressive forces, thereby reducing the critical buckling load.

For P_z>0, the $\overline{N}_{cr}$ also reduces, however the reduction is less pronounced than that of P_x. This indicates that transverse material gradation influences bending stiffness to a greater extent than axial stiffness. At L/h=5 and P_x=0, the $\overline{N}_{cr}$ decreases from 12.569 (P_z=0) to 3.317 (P_z=5). For L/h=20 and P_x=0, the $\overline{N}_{cr}$ decreases from 13.132 (P_z=0) to 3.429 (P_z=5). By controlling the value of P_z, the bending stiffness reduces because the material ratio changes from the outer layer of the beam to the inner part. This makes the beam more sensitive to buckle when subjected to compressive load. However, since axial stiffness has a more significant impact on buckling behavior, the influence of P_z is less dominant than P_x.

The above analysis shows that the values of the $\overline{N}_{cr}$ are reducing as $L/_h$ increases across all the variations of P_x and P_z. Although, this persistent tendency emphasizes structural stability has been dominated entirely by geometry. Reducing P_x by setting P_x=0 and P_z=0 results in a decline in the $\overline{N}_{cr}$ from 12.569 for $L/_h$=5 to 13.132 for $L/_h$=20. For P_x=5 and P_z=5, there is distribution reduction from 1.848 ($L/_h$=5) to 1.911 ($L/_h$=20). Higher L/h ratios represent slender beams that have reduced resistance to buckling due to their higher susceptibility to lateral deformation under axial loads (Wu *et al*. 2024). The effect of aspect ratio is particularly pronounced under CF boundary conditions because the free end offers no restraint that further amplifies the instability of slender beams. The $\overline{N}_{cr}$ of the CF FGPB at various P_x, P_z and $L/_h$ is presented as Table 6.

4.3 Effect of porosity on dimensionless critical buckling

The porosity of a material influences the stiffness, density, and stability. The nature of porosity, even or uneven, plays a critical role in determining the behavior of the beam under loading conditions and in buckling analysis. Even porosity assumes a uniform distribution of pores throughout the volume of the beam and simplifies the modeling and analysis. Uneven porosity denotes the non-uniform distribution of pores, characterized by the coexistence of areas of varying stiffness inside the beam. This distribution more precisely reflects real-world materials, where pores are concentrated areas due to production methods or functional necessities.

The effect of porosity distribution and porosity index (P_x, Pz) on the $\overline{N}_{cr}$ under SS boundary conditions at $L/_h$=5 is illustrated in Figs. 8(a) and (b). The $\overline{N}_{cr}$ decreases across all porosity indexes (α) and porosity types (even or uneven) with an increase in P_x. This indicates that higher longitudinal gradient reduces the stability of the beam under compressive loads. For instance, for α=0.1 with even porosity and P_z=0, the $\overline{N}_{cr}$ reduces from 51.342 (P_x=0) to 10.844 (P_x=5). A comparable pattern is noted for uneven porosity, as the $\overline{N}_{cr}$ reduces from 60.827 (P_x=0) to 12.851 (P_x=5). Increasing P_x shifts the material composition along the length of the beam from a stiff ceramic region to a more flexible metallic region that significantly reduces axial stiffness. The $\overline{N}_{cr}$ also decreases with increasing P_z across all conditions rather, the reduction is less steep compared to P_x (Shabani *et al*. 2024). For instance, at α=0.1 with even porosity and P_x=0, the $\overline{N}_{cr}$ decreases from 51.342 (P_z=0) to 14.410 (P_z=5). The $\overline{N}_{cr}$ decreases from 60.827 (P_z=0) to 18.537 (P_z=5) in uneven porosity. Conversely, P_z affects the bending stiffness by altering the material distribution through the thickness of the beam. As bending stiffness is of less significance in buckling, its reduction with P_z is less evident than with P_x.

Even porosity is seen to yield a lower critical buckling load compared to uneven porosity under similar conditions. For example, when α=0.1 and P_x=0 the $\overline{N}_{cr}$ is found to be 51.342 for even porosity and 60.827 for uneven porosity. For instance, when α=0.1 and P_x=0, the $\overline{N}_{cr}$ is 51.342 for even porosity and 60.827 for uneven porosity. This trend remains consistent for all gradient indices and porosity range values as well. Even porosity takes the form of a geometrical distribution where there is complete randomness of pores all over the side of the material causing a similar reduction in the rigidity of the material. This uniform weakening leads to lower $\overline{N}_{cr}$

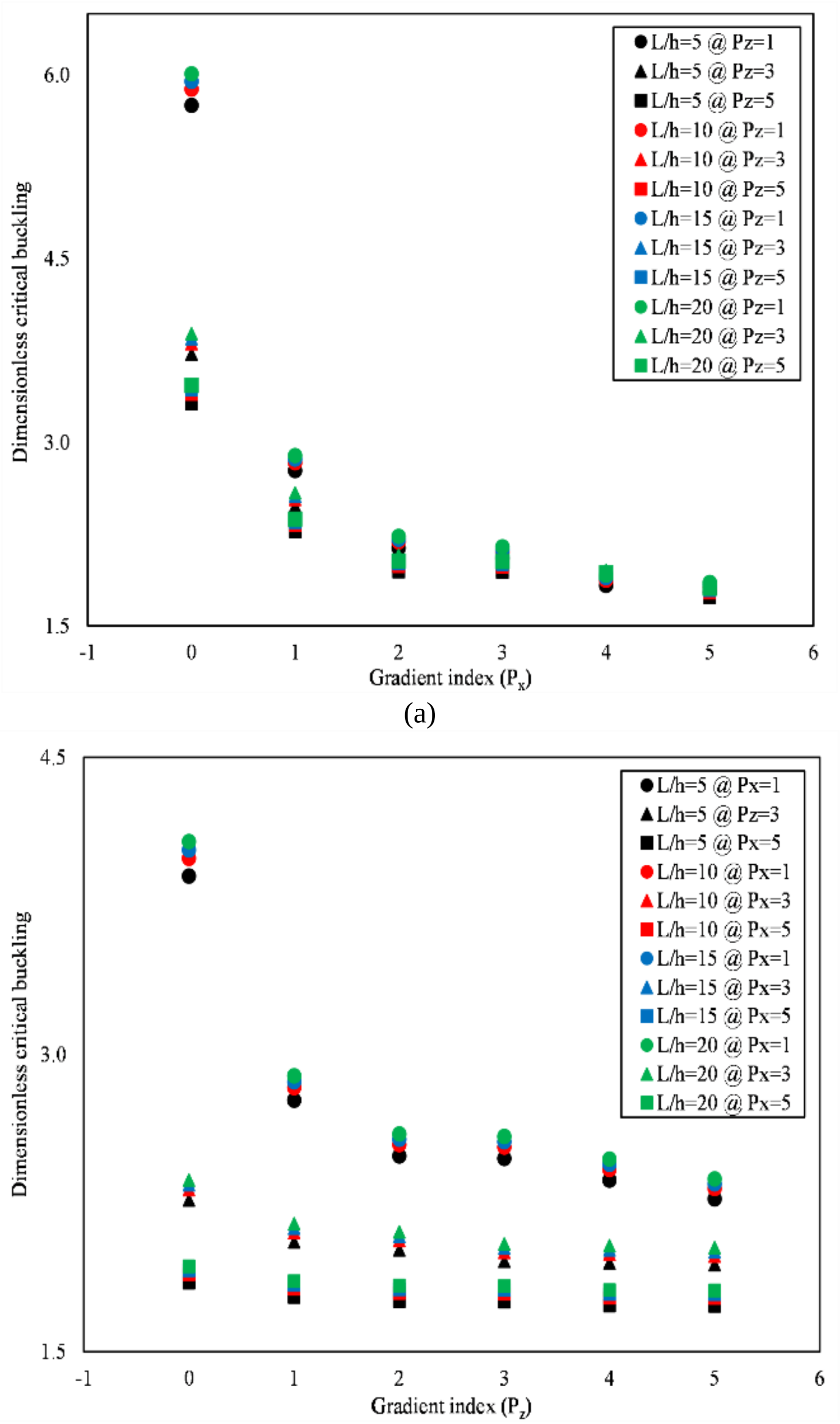

(a)

(b)

Fig. 7 The effect of gradient indexes, (a) P_x, and (b) P_z on the $\overline{N}_{cr}$ at various aspect ratios under CF boundary conditions

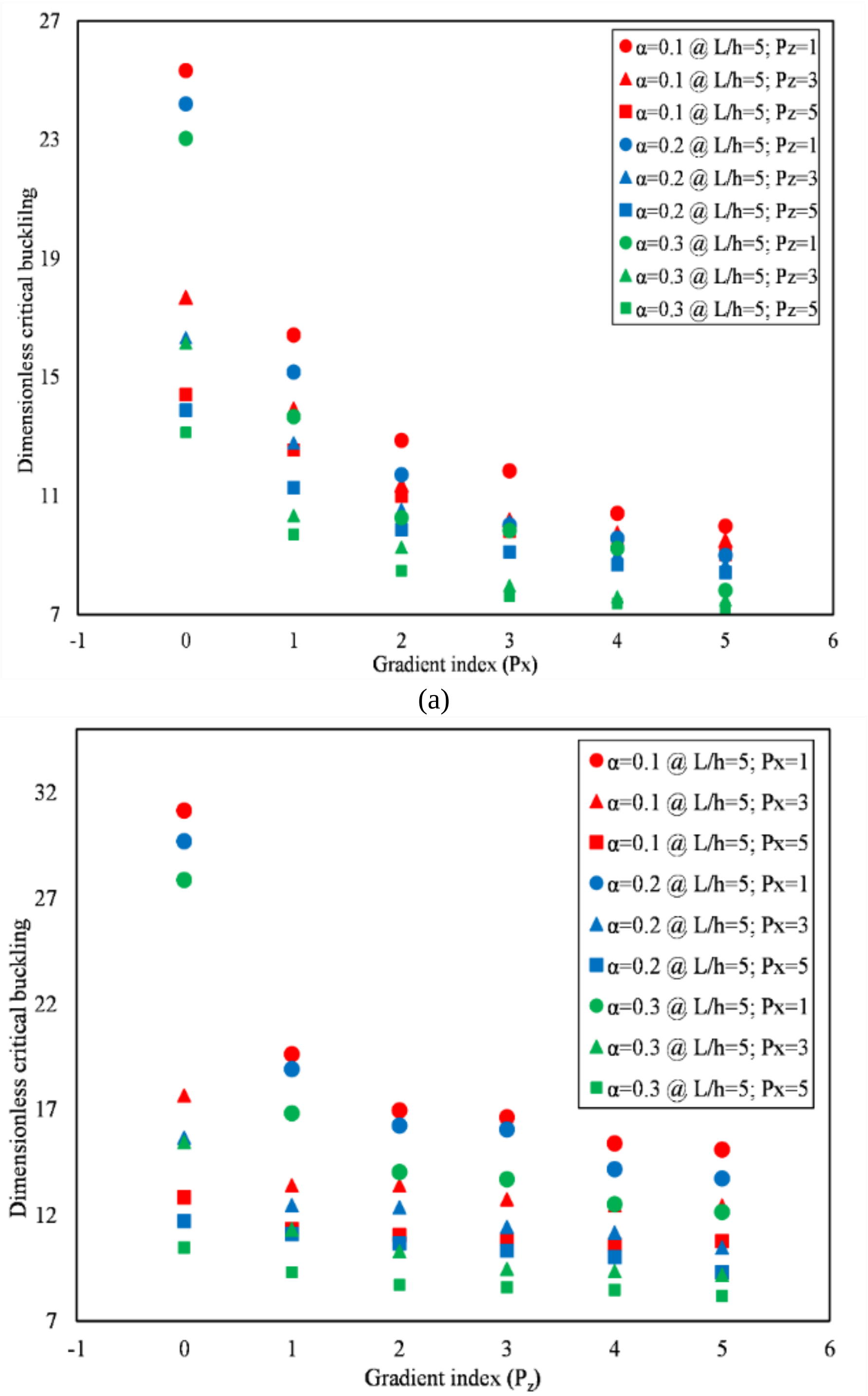

(a)

(b)

Fig. 8 The effect of porosity distribution, (a) Even, and (b) Uneven on the dimensionless critical buckling at various aspect ratios under SS boundary conditions

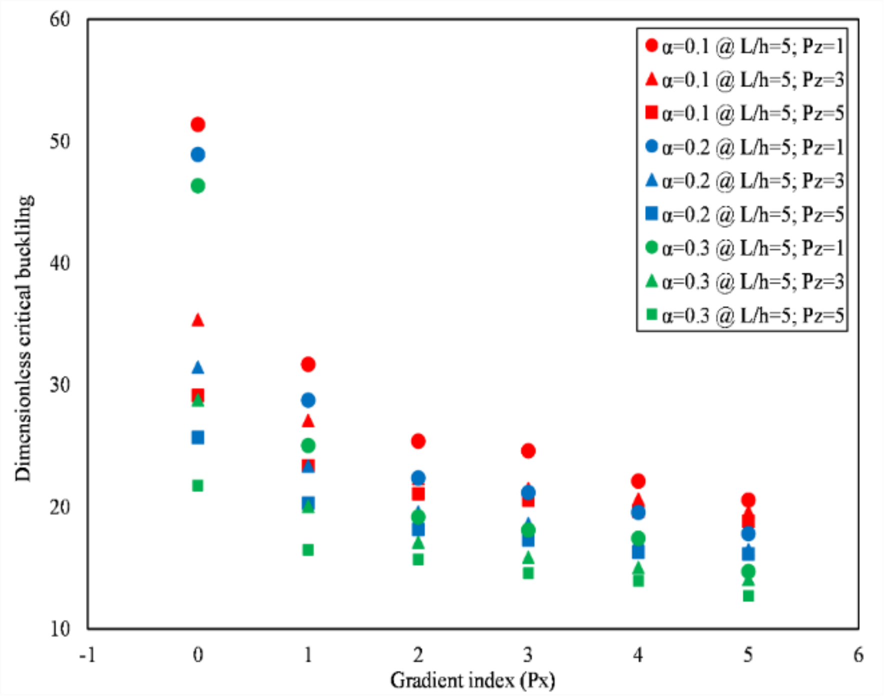

(a)

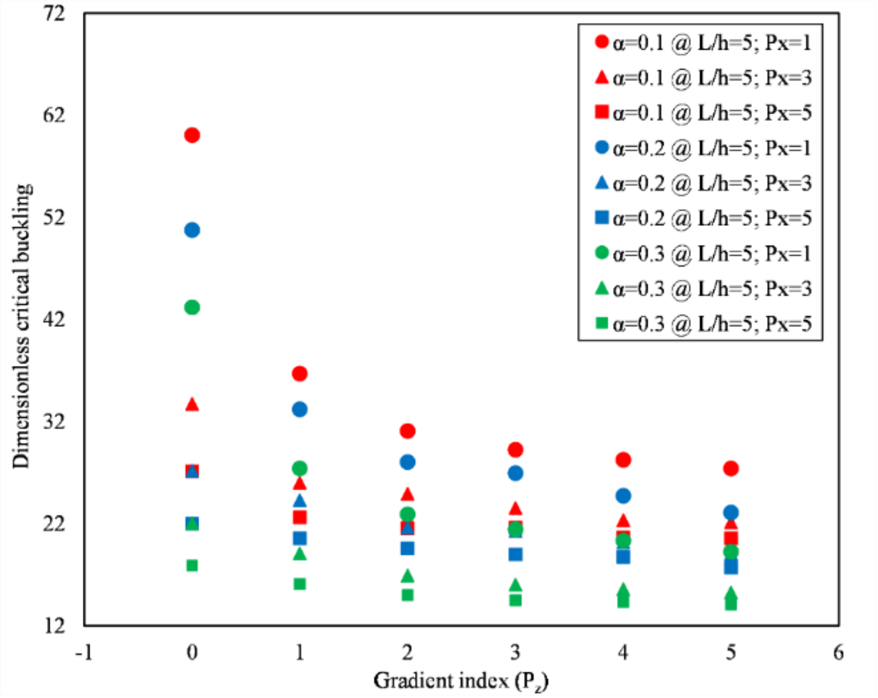

(b)

Fig. 9 The effect of porosity distribution, (a) Even, and (b) Uneven on the dimensionless critical buckling at various aspect ratios under CS boundary conditions compared to uneven porosity where the material stiffness may be in areas that offer higher compression resistance. Uneven porosity shows higher $\overline{N}_{cr}$ under all conditions due to the non-uniform distribution of pores. For example, when α=0.2 and P_x=0, the $\overline{N}_{cr}$ is 50.446 for even porosity and 59.837 for uneven porosity. Uneven porosity has localized areas of higher stiffness which in turn give the beam capability to resist compressive force (Bridjesh *et al*. 2023). This distribution helps in reducing the detrimental effects of pore on the general structural integrity which leads to improved buckling resistance than porous uniform materials.

The effect of porosity distribution and porosity index (P_x, Pz) on the $\overline{N}_{cr}$ under CS boundary conditions $^{L}/_{h}$=5 is illustrated in Figs. 9(a) and (b). The $\overline{N}_{cr}$ decreases significantly as P_x increases across all porosity levels (α) and distributions. For α=0.1 with even porosity and P_z=0, the $\overline{N}_{cr}$ decreases from 101.656 (P_x=0) to 23.052 (P_x=5). When the porosity is uneven, the $\overline{N}_{cr}$ drops from 127.424 (P_x=0) to 27.125 (P_x=8) in a similar way. Increasing P_x introduces a longitudinal material gradient that transitions the beam from stiffer ceramic regions to more flexible metallic regions along its length. This reduces the axial stiffness, the principal resistance mechanism against buckling, resulting in a reduced $\overline{N}_{cr}$. The $\overline{N}_{cr}$ decreases across all conditions as Pz increases. The $\overline{N}_{cr}$ decreases from 99.500 (P_z=0) to 25.693 (P_z=5) for α=0.2 with even porosity and P_x=0. Similarly, with uneven porosity, the $\overline{N}_{cr}$ decreases from 120.795 (P_z=0) to 29.085 (P_z=5). Increasing P_z affects the bending stiffness by altering the material composition across the beam thickness. The loss in bending resistance makes the beam more susceptible to deformation under axial loads and its effect is less significant than P_x since axial stiffness dominates in buckling behavior.

Even porosity consistently results in lower $\overline{N}_{cr}$ compared to uneven porosity. For α=0.1, P_x=0 and P_z=0, the $\overline{N}_{cr}$ is 101.656 for even porosity and 127.424 for uneven porosity. Even porosity implies a uniform pore distribution throughout the beam. This uniform weakening reduces both axial and bending stiffness that makes the beam less resistant to compressive loads. The loss in stiffness is consistent and more detrimental compared to uneven porosity. Uneven porosity exhibits higher buckling loads under all conditions due to the non-uniform distribution of pores. For α=0.2, P_x=0 and P_z=0, the $\overline{N}_{cr}$ is 99.500 and 120.795 for even porosity and uneven porosity, respectively. When porosity is uneven, there are areas that are stiffer and can resist compression forces.

The effect of porosity distribution and porosity index (P_x, Pz) on the $\overline{N}_{cr}$ under CC boundary conditions $^{L}/_{h}$=5 is illustrated in Figs. 10(a) and (b). The $\overline{N}_{cr}$ decreases significantly as P_x increases across all porosity levels and distributions. The $\overline{N}_{cr}$ decreases from 101.656 (P_x=0) to 23.052 (P_x=5) when α=0.1 when the porosity is even. A similar trend is observed for uneven porosity, where the $\overline{N}_{cr}$ drops from 127.424 (P_x=0) to 27.125 (P_x=5). Increasing P_x introduces a longitudinal material gradient that transitions the beam from stiffer ceramic regions to more flexible metallic regions along its length (Bridjesh *et al*. 2024). This weakens the axial stiffness that is the primary resistance mechanism against buckling which leads to a lower $\overline{N}_{cr}$.

The $\overline{N}_{cr}$ decreases across all conditions as P_z increases. For α=0.2 with even porosity and P_x=0, the $\overline{N}_{cr}$ decreases from 99.500 (P_z=0) to 25.693 (P_z=5). Similarly, with uneven porosity, the $\overline{N}_{cr}$ decreases from 120.795 (P_z=0) to 29.085 (P_z=5). Increasing Pz affects the bending stiffness by altering the material composition across the beam thickness, Nathi (2022). The loss in bending resistance makes the beam more susceptible to deformation under axial loads and its effect is less significant than P_x since axial stiffness dominates in buckling behavior.

The effect of porosity distribution and porosity index (P_x, Pz) on the $\overline{N}_{cr}$ under CF boundary

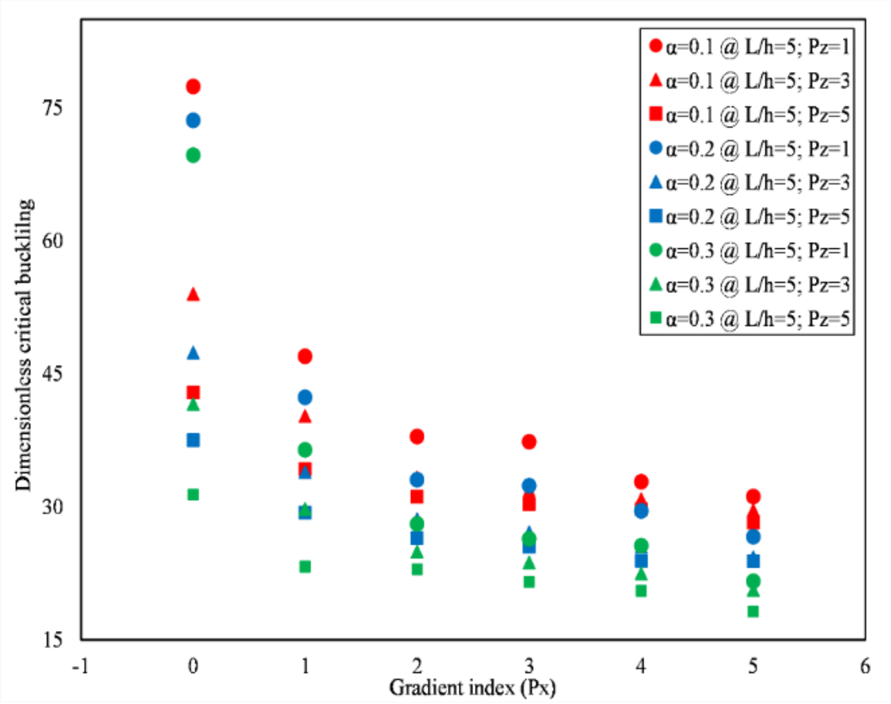

(a)

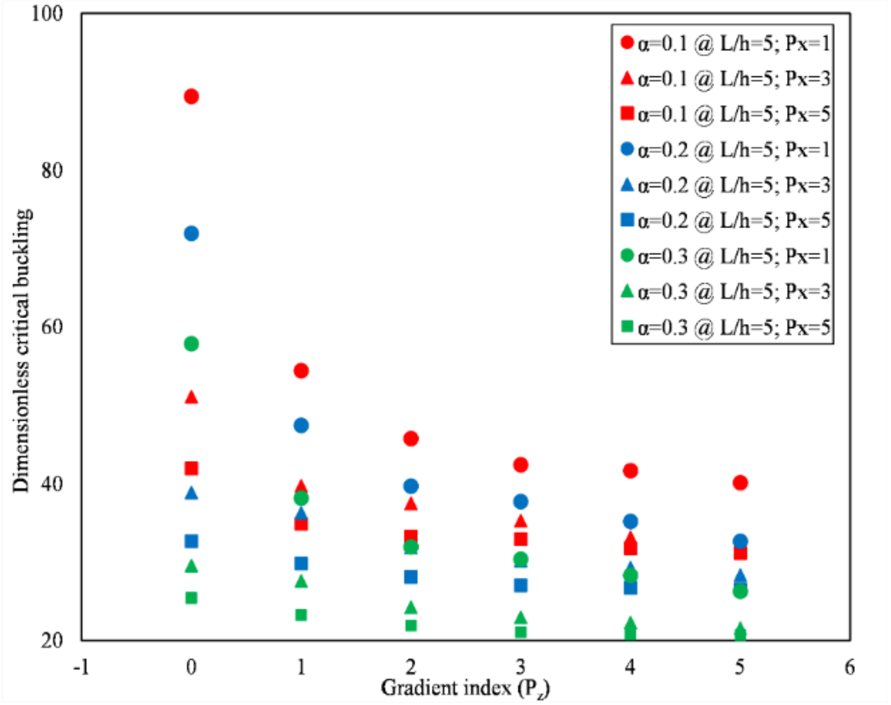

(b)

Fig. 10 The effect of porosity distribution, (a) Even, and (b) Uneven on the dimensionless critical buckling at various aspect ratios under CC boundary conditions

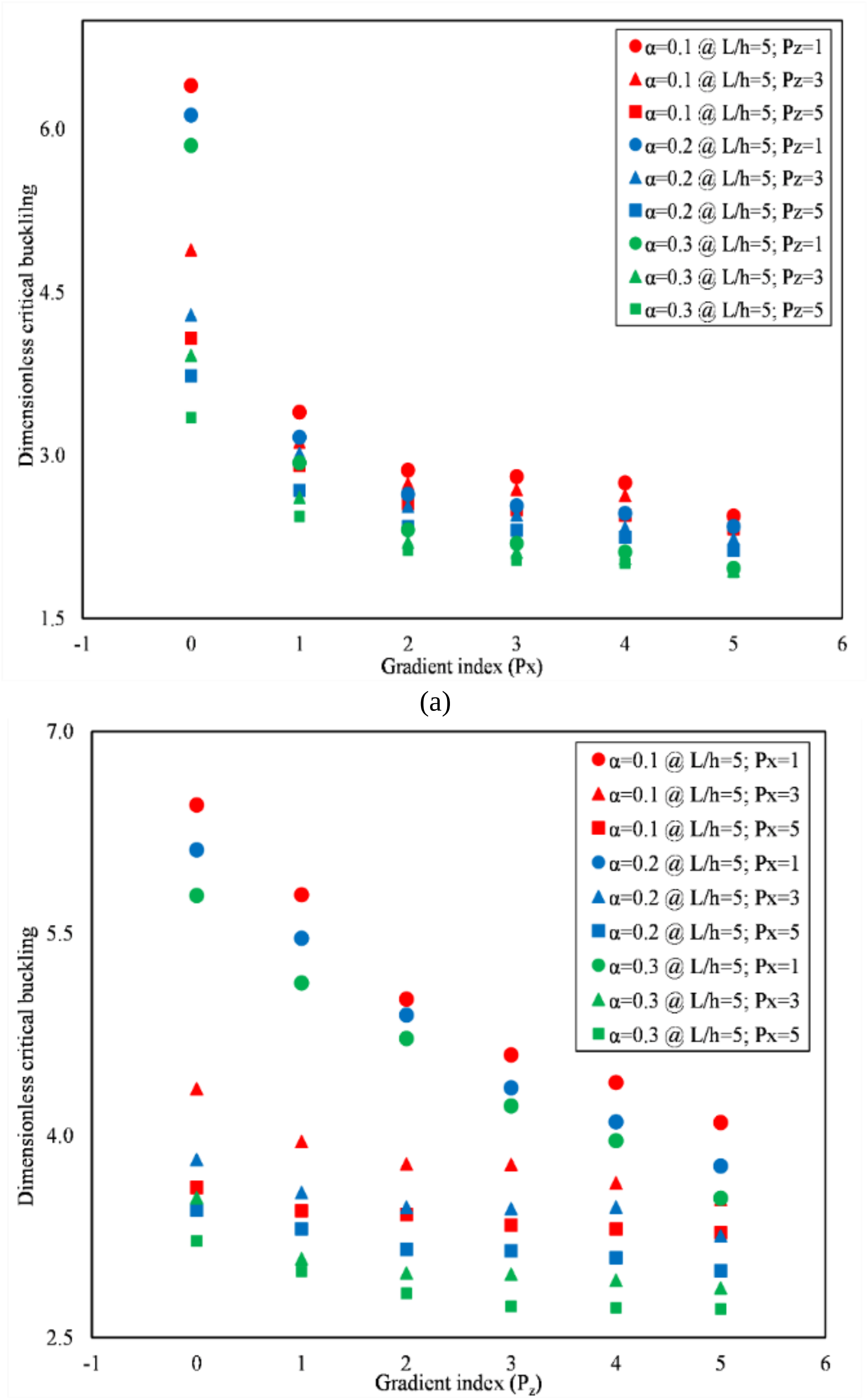

(a)

(b)

Fig. 11 The effect of porosity distribution, (a) Even, and (b) Uneven on the dimensionless critical buckling at various aspect ratios under CF boundary conditions

conditions $L/_h$=5 is illustrated in Figs. 11(a) and (b). The $\bar{N}_{cr}$ decreases as P_x increases across all porosity levels and distributions. The $\bar{N}_{cr}$ drops from 13.175 (P_x=0) to 2.564 (P_x=5) when α=0.1 and P_z=0 under even porosity conditions. The $\bar{N}_{cr}$ decreases from 18.571 (P_x=0) to 3.614 (P_x=5) under uneven porosity distribution for the same conditions. In the buckling analysis of porous beam, Turan and Adiyaman (2024) found the values of $\bar{N}_{cr}$ under even porosity conditions as 2.7065 at P_x=1, P_z=1 and 1.9901 at P_x=2, P_z=2. Whereas, in the present study, the values are 2.769 and 2.036.

The material becomes less stiff along the length of the beam due to an increasing metallic composition as P_x increases. This reduction in axial stiffness makes the beam more vulnerable to buckling under compressive forces that is a dominant factor in CF boundary conditions. Increasing P_z reduces the $\bar{N}_{cr}$ and the effect is less pronounced compared to P_x. The $\bar{N}_{cr}$ drops from 12.976 (P_z=0) to 3.731 (P_z=5) when α=0.2 and the porosity is even. The $\bar{N}_{cr}$ decreases from 18.291 (P_z=0) to 5.560 (P_z=5) for uneven porosity distribution. Higher Pz decreases the bending stiffness by altering the material distribution through the thickness of the beam, Nathi (2022). Bending stiffness is a secondary factor in CF buckling and its reduction contributes to a moderate decline in critical buckling load.

Even porosity resulted in lower $\bar{N}_{cr}$ as compared to uneven porosity under the same conditions. At α=0.1, P_x=0, and P_z=0, the $\bar{N}_{cr}$ is 13.175 for even porosity and 18.571 for uneven porosity. Uneven porosity exhibits higher buckling loads across all conditions. From the above results, it is identified that even and uneven porosity distributions the value of $\bar{N}_{cr}$ is nearly 12.976 and 18.291 respectively at α=0.2, P_x=0, P_z=0. Uneven porosity allows for non-uniform distribution of pores that concentrate stiffness in specific regions of the beam (Bridjesh *et al.* 2023). This localized reinforcement offsets the adverse effects of pores that maintain higher axial and bending stiffness compared to evenly porous materials.

Porosity distribution and porosity index significantly influence the dimensionless critical buckling load across all boundary conditions by altering the structural stiffness and stability of the beam. Even porosity is characterized by a uniform pore distribution that exhibits lower critical buckling loads due to homogeneous weakening of both axial and bending stiffness. This renders even porosity less advantageous for structural applications necessitating greater buckling resistance. Uneven porosity exhibits a non-uniform pore distribution that demonstrates higher buckling loads under all boundary conditions. The localized stiffness reinforcement in uneven porosity effectively offsets the adverse effects of pores that maintain greater axial and bending stiffness and enhancing structural stability.

The critical buckling load decreases for both even and uneven porosity distributions with an increase in the porosity index that represents a higher pore volume fraction. The reduction is more significant under less restrictive boundary conditions, such as CF and SS, because of their greater vulnerability to axial and lateral deformations. CC boundary conditions yield the best buckling loads for all the porosity distributions and indexes since it is the most restrictive. The combined analysis of porosity type and porosity index underlines the importance of effective control over the porosity characteristics providing both lightweight and mechanical reinforcement of FGPB.

5. Conclusions

This study provides the analysis of buckling characteristics of FGPB using the boundary conditions of SS, CS, CC, and CF. The FGPB is modelled adapting HSDT and the KKT conditions for solving the governing equations. The analysis considers the effect of gradient indices (P_x, Pz), porosity distributions (even as well as uneven) and porosity index (α) on the dimensionless critical buckling load. The findings emphasize the pivotal role of material gradation and porosity distribution in determining the buckling performance of FGPB. The key findings of this study are as follows:

- The results show good agreement with previously published literature with deviations under 5% that confirm the accuracy and robustness of the proposed methodology.
- KKT conditions could integrate various constraints related to gradation and porosity distributions to properly assess the structural stability.
- The analysis of buckling mode shapes for SS, CS, CC, and CC boundary conditions shows that the deformation of CC is confined and most stable. Specifically, for a homogeneous CC beam, the mode forms show symmetric characteristics to the mid-point of the beam. On the other hand, CF is highly vulnerable to instability due to minimal boundary conditions.
- The impact of shear deformation on the critical buckling load is demonstrated to increase with an increase in the aspect ratio for the specified gradient index. However, the shear deformation of CC beam is much higher when compared with the deformations of other types of beams. The dimensionless critical buckling load for SS, CS, CC, and CF boundary conditions at $^{L}/_{h}$=5 was found to be 51.342, 102.318, 153.295, and 12.569, respectively, and at $^{L}/_{h}$=20 was, 59.684, 113.282, 170.418, and 13.132, respectively.
- The gradient indices significantly influence the dimensionless buckling load of the FGPB. An increase in the longitudinal gradient index leads to a significant reduction in the critical buckling load. Under SS boundary conditions with α=0.1 and Pz=0, the buckling load decreases from 51.342 at P_x=0 to 10.844 at P_x=5. The same tendency can be noticed for the transverse gradient index as well, even though the impact of the transverse gradient index is not as significant as the longitudinal gradient index.
- The influence of porosity distribution on the critical buckling load of the even and uneven FGPB may depend on the kind of boundary condition provided to the beam. Even porosity distribution results in lower critical buckling loads compared to uneven porosity. Under CC boundary conditions at α=0.1, P_x=0, and P_z=0, the dimensionless critical buckling load for even and uneven porosity distribution were found to be 151.970 and 196.587, respectively.
- The dimensionless critical buckling for both even and uneven porosity distributions decreases with an increase in the porosity index. Under CS boundary conditions with P_x=0 and P_z=0, the dimensionless critical buckling reduced from 101.656 at α=0.1 to 97.314 at α=0.3 under even porosity, and from 127.424 to 114.555 under uneven porosity.
- The CC configuration yield the highest dimensionless critical buckling loads among all boundary conditions, followed by CS, SS, and CF. With α=0.1 with P_x=0 and P_z=0, the dimensionless critical buckling load is 151.970 for CC, 101.656 for CS, 51.342 for SS, and 13.175 for CF indicating that the boundary conditions significantly influence the stability of the beam.

The present study demonstrates the effect of gradient indices, porosity distributions, porosity indices and boundary conditions are crucial in determining the buckling response of FGPB. The implementation of KKT conditions offers a mathematical basis for the solution of the governing equations that ensure proper and effective computations for different geometries. The findings of this analysis offer a platform for the enhancement of material gradation and porosity distribution for the improvement of structural efficiency and performance. The effects of dynamic loading, thermal stress and environmental factors in the stability of FGPB can be considered for future investigations. The use of Machine Learning models in the estimation of the buckling loads of FGPB with complex geometries and varying material distribution can be a possible replacement for conventional approaches.

References

Adiyaman, G. and Turan, M. (2024), “Bending and buckling analysis of porous 2D functionally graded beams with exponential material property variation”, *Iran. J. Sci. Technol. Transact. Civil Eng.*, 1-28. https://doi.org/10.1007/s40996-024-01508-4

Amandeep singh, S.J. and Padhee, S.S. (2024), “Analytic solution of timoshenko-like deformation in bidirectional functionally graded beams”, *J. Eng. Mech.*, **150**(2), 04023118. https://doi.org/10.1061/JENMDT.EMENG-7317

Amir, M. and Kim, S.W. (2024), “A study of the natural frequencies of the functionally graded curved beams including porosities: deterministic and stochastic modeling”, *Mech. Based Des. Struct.*, **52**(8), 5970-5987. https://doi.org/10.1080/15397734.2023.2266828

Benmalek, H., Bouziane, S., Bouzerd, H. and Suleiman, H. (2024), “Innovative mixed finite element method for bending analysis of functionally graded beams: modelling, validation, and applications”, *Eng. Res. Express*, **6**(1), 015055. https://doi.org/10.1088/2631-8695/ad1f16

Bridjesh, P., Geetha, N.K. and Yelamasetti, B. (2024), “Numerical investigation on buckling of two-directional porous functionally graded beam using higher order shear deformation theory”, *Int. J. Interact. Des. Manuf.*, **18**(5), 2805-2818. https://doi.org/10.1007/s12008-023-01332-6

Bridjesh, P., Geetha N.K. and Reddy, G.C.M. (2023), “On numerical investigation of buckling in two-directional porous functionally graded beam using higher order shear deformation theory”, *Mech. Adv. Compos. Struct.*, **10**(2), 393-406. https://doi.org/10.22075/macs.2023.29340.1462

Chandel, V.S. and Talha, M. (2024), “The random thermo-elastic nonlinear vibration analysis of porous fgm nano-beams using the first order perturbation theory”, *Proceedings of the Institution of Mechanical Engineers*, *Part C: Journal of Mechanical Engineering Science*, **238**(11), 5241-5257. https://doi.org/10.1177/09544062231212324

Chen, D., Gao, K., Yang, J. and Zhang, L. (2023), “Functionally graded porous structures: Analyses, performances, and applications–a review”, *Thin Wall. Struct.*, **191**, 111046. https://doi.org/10.1016/j.tws.2023.111046

Chen, D., Wang, Y., Zheng, S., Liang, Y. and Sun, S. (2024), “Isogeometric analysis of bi-directional functionally graded porous micro-beam with geometrical imperfections using nonlocal strain gradient theory”, *J. Vib. Eng. Technol.*, **12**(Suppl 1), 1031-1043. https://doi.org/10.1007/s42417-024-01460-7

Chintalapudi, R., Kannaiyan, G. N., Pappula, B. and Makgato, S. (2024), “The novel vogel's approximation method integrated with a random forest algorithm in the vibration analysis of a two-directional functionally graded taper porous beam: assessment”, *Sci. African*, **26**, e02397. https://doi.org/10.1016/j.sciaf.2024.e02397

Chintalapudi, R., Kannaiyan, G.N., Pappula, B. and Makgato, S. (2024), “The effects of gradient index, aspect ratio, porosity, and boundary conditions on the buckling behavior of functionally graded porous beams: a k-out-of-n system reliability analysis”, *Results Phys.*, **60**, 107634. https://doi.org/10.1016/j.rinp.2024.107634

Derikvand, M., Farhatnia, F. and Hodges, D.H. (2023), “Functionally graded thick sandwich beams with porous core: Buckling analysis via differential transform method”, *Mech. Based Des. Struct.*, **51**(7), 3650-3677. https://doi.org/10.1080/15397734.2021.1931309

Deng, Z. and Shang, Y. (2024), “Size-dependent finite element analysis of functionally graded flexoelectric shell structures based on consistent couple stress theory”, *Aerospace*, **11**(8), 661. https://doi.org/10.3390/aerospace11080661

Feng, M., Li, S. and Wang, J. (2022), “On tucker-type alternative theorems and necessary optimality conditions for nonsmooth multiobjective optimization", *J. Opt. Theory Appl.*, **195**(2), 480-503. https://doi.org/10.1007/s10957-022-02092-1

Gao, K., Huang, H., Zou, Z., Wu, Z., Zhu, H. and Yang, J. (2024), "Buckling analysis of multi-span non-uniform beams with functionally graded graphene-reinforced foams", *Int. J. Mech. Sci.*, **263**, 108777. https://doi.org/10.1016/j.ijmecsci.2023.108777

Geetha, N.K., Bridjesh, P., Yelamasetti, B., Saxena, K.K. and Gupta, N. (2023), "Analytical modelling of a multifunctional heterogeneous beam-bending analysis", *Proceedings of the Institution of Mechanical Engineers*, *Part E: Journal of Process Mechanical Engineering*, 09544089231207421. https://doi.org/10.1177/09544089231207421

Ghatage, P. S., Kar, V.R. and Sudhagar, P.E. (2020), "On the numerical modelling and analysis of multi-directional functionally graded composite structures: A review", *Compos. Struct.*, **236**, 111837. https://doi.org/10.1016/j.compstruct.2019.111837

Hasim, K.A. and Kefal, A. (2024), "Free and forced vibration analysis of piezolaminated plates via an isogeometric layerwise finite element", *Mech. Adv. Mater. Struct.*, 1-16. https://doi.org/10.1080/15376494.2024.2400716

Indronil, D. (2024), "Bending of bidirectional functionally graded nonlocal stress-driven beam", *Heliyon*, **10**(17). https://doi.org/10.1016/j.heliyon.2024.e36513

Jain, R., Azam, M.S. and Singh, P.P. (2024), "Bending analysis of functionally graded plates resting on elastic foundation: A rayleigh-ritz approach and ann method", *Mech. Adv. Mater. Struct.*, **31**(29), 11484-11502. https://doi.org/10.1080/15376494.2024.2307474

Jiao, Z., Wang, G., Xu, R., Chen, W. and Reddy, J.N. (2024), "Free vibration and buckling analysis of functionally graded beams using the dmcdm", *Compos. Struct.*, **332**, 117905. https://doi.org/10.1016/j.compstruct.2024.117905

Karamanlı, A. (2018), "Analytical solutions for buckling behaviour of two directional functionally graded beams using a third order shear deformable beam theory", *J. Eng. Sci.*, **6**(2), 164-178. https://doi.org/10.21541/apjes.357539

Kumar, A.S., Kumar, S., Choudhary, P.K., Gupta, A. and Narayan, A. (2024), "Free vibration characteristics of elastic foundation-supported porous functionally graded nanoplates using rayleigh-ritz approach", *Int. J. Struct. Integr.*, **15**(2), 298-321. https://doi.org/10.1108/IJSI-11-2023-0114

Kumar, S., Roy, H., Mitra, A. and Ganguly, K. (2024), "Dynamic analysis of bi-directional functionally graded beam with geometric nonlinearity", *J. Vib. Eng. Technol.*, **12**(3), 3051-3067. https://doi.org/10.1007/s42417-023-01032-1

Li, X. and Hu, X. (2024), "Algebraically stable high-order multi-physical property-preserving methods for the regularized long-wave equation", *Appl. Numer. Math.*, **203**, 144-150. https://doi.org/10.1016/j.apnum.2024.05.022

Liang, Y., Zheng, S., Wang, H. and Chen, D. (2024), "Nonlinear isogeometric analysis of axially functionally graded graphene platelet-reinforced composite curved beams", *Compos. Struct.*, **330**, 117871. https://doi.org/10.1016/j.compstruct.2023.117871

Le, Q.C., Nguyen, N.D. and Vo, T.P. (2024), "A novel hybrid function-based ritz method for static and free vibration of axially loaded bi-directional functionally graded porous beams", *Mech. Based Des. Struct.*, 1-29. https://doi.org/10.1080/15397734.2024.2407418

Lore, S., Deshpande, A.S. and Singh, B.N. (2024), "Nonlinear free vibration analysis of functionally graded plates and shell panels using quasi-3d higher order shear deformation theory", *Mech. Adv. Mater. Struct.*, **31**(2), 453-469. https://doi.org/10.1080/15376494.2022.2114050

Ma, X., Zhou, B., Li, C., Zhang, Y., Yang, M. and Xue, S. (2024), "Analysis of functionally graded piezoelectric structures by hermite interpolation element-free galerkin method", *J. Intell. Mater. Syst. Struct.*, **35**(12), 1019-1039. https://doi.org/10.1177/1045389X241233800

Miyamoto, Y., Kaysser, W.A., Rabin, B.H., Kawasaki, A. and Ford, R.G. (1999), *Functionally Graded Materials: Design*, *Processing and Application*, Kluwer Academic Publishers, London, U.K.

Nathi, V.K. (2022), "Buckling analysis of 2d functionally graded porous beams using novel higher order theory", *J. Comput. Appl. Mecha.*, **53**(3), 393-413. https://doi.org/10.22059/jcamech.2022.345384.736

Nguyen, N.D., Nguyen, T.N., Nguyen, T.K. and Vo, T.P. (2022), “A new two-variable shear deformation theory for bending, free vibration and buckling analysis of functionally graded porous beams”, *Compos. Struct.*, **282**, 115095. https://doi.org/10.1016/j.compstruct.2021.115095

Nguyen, N.D. (2024), “A new higher-order beam theory for buckling and free vibration responses of laminated composite and functionally graded porous beams”, *J. Strain Anal. Eng. Des.*, **59**(1), 67-81. https://doi.org/10.1177/03093247231187454

Nguyen, M.N., Lee, D., Kang, J. and Shin, S. (2023), “Topology optimization with functionally graded multi-material for elastic buckling criteria”, *Steel Compos. Struct.*, **46**(1), 33-51. https://doi.org/10.12989/scs.2023.46.1.033

Nguyen, V.L., Tran, M.T., Chu, T.B., Nguyen, T.A. and Nguyen, V.L. (2024), “Nonlinear dynamic response of functionally graded porous beams under a moving mass using reddy’s beam theory”, *Iran. J. Sci. Technol. Transact. Mech. Eng.*, **48**(3), 1205-1221. https://doi.org/10.1007/s40997-023-00705-2

Patil, H.H., Pitchaimani, J. and Eltaher, M.A. (2024), “Buckling and vibration of beams using ritz method: effects of axial grading of gpl and axially varying load”, *Mech. Adv. Mater. Struct.*, **31**(16), 3861-3874. https://doi.org/10.1080/15376494.2023.2185711

Qiu, N., Zhang, J., Li, C., Shen, Y. and Fang, J. (2023), “Mechanical properties of three-dimensional functionally graded triply periodic minimum surface structures”, *Int. J. Mech. Sci.*, **246**, 108118. https://doi.org/10.1016/j.ijmecsci.2023.108118

Rajasekaran, S. (2024), “Torsion analysis of functionally graded iso/orthotropic sections using differential quadrature and pb2-rayleigh ritz methods”, *J. Inst. Eng. Series A*, 1-38. https://doi.org/10.1007/s40030-024-00833-1

Reddy, G., Bridjesh, P., Reddy, B.S. and Reddy, K.V.K. (2024), “Comparison of deflection in two-directional functionally graded tapered beam”, *Mech. Adv. Compos. Struct.*, **11**(1), 191-202. https://doi.org/10.22075/macs.2023.29871.1478

Shabani, Y., Mehdianfar, P. and Khorshidi, K. (2024), “Static buckling and free vibration analysis of bi-dimensional fg metal ceramic porous beam”, *Mech. Adv. Compos. Struct.*, **11**(1), 149-158. https://doi.org/10.22075/macs.2023.29847.1476

Sun, S.L., Zhang, X.Y. and Li, X.F. (2024), “A consistent shear beam theory for free vibration of functionally graded beams based on physical neutral plane”, *Mech. Adv. Mater. Struct.*, **31**(16), 3844-3854. https://doi.org/10.1080/15376494.2023.2185709

Taghizadeh, M., Babaei, M., Dimitri, R. and Tornabene, F. (2024), “Assessment of critical buckling load of bi-directional functionally graded truncated conical micro-shells using modified couple stress theory and ritz method”, *Mech. Based Des. Struct.*, **52**(6), 3456-3487. https://doi.org/10.1080/15397734.2023.2202230

Turan, M. and Adiyaman, G. (2024), “Free vibration and buckling analysis of porous two-directional functionally graded beams using a higher-order finite element model”, *J. Vib. Eng. Technol.*, **12**(1), 1133-1152. https://doi.org/10.1007/s42417-023-00898-5

Wang, S., Qian, Z. and Shang, Y. (2024), “Size-dependent finite element analysis of fgms in thermal environment based on the modified couple stress theory”, *Eng. Comput.* https://doi.org/10.1108/EC-10-2023-0666

Wu, C.P. and Huang, Z. (2024), “A unified consistent couple stress beam theory for functionally graded microscale beams”, *Steel Compos. Struct.*, **51**(2), 103-116. https://doi.org/10.12989/scs.2024.51.2.103

Wu, S., Li, Y., Bao, Y., Zhu, J. and Wu, H. (2024), “Examination of beam theories for buckling and free vibration of functionally graded porous beams”, *Materials*, **17**(13), 3080. https://doi.org/10.3390/ma17133080

Xu, Z., Zhang, L., Xu, R., Chen, W. and Wang, G. (2024), “Static, dynamic and buckling behavior of functionally graded beams with tunable inclusions”, *Int. J. Solids Struct.*, **288**, 112620. https://doi.org/10.1016/j.ijsolstr.2023.112620

Yaylacı, M., Abanoz, M., Yaylacı, E.U., Ölmez, H., Sekban, D.M. and Birinci, A. (2022), “The contact problem of the functionally graded layer resting on rigid foundation pressed via rigid punch”, *Steel Compos. Struct.*, **43**(5), 661-672. https://doi.org/10.12989/scs.2022.43.5.661

Yu, J. (2024), "Discrete variational method for partial differential equations of functionally gradient beam vibration", *J. Comput. Meth. Sci. Eng.*, **24**(4-5), 2957-2971. https://doi.org/10.3233/JCM-247536

Zhao, Y.F., Gao, Y.S., Wang, X., Markert, B. and Zhang, S.Q. (2024), "Finite element analysis of functionally graded magneto-electro-elastic porous cylindrical shells subjected to thermal loads", *Mech. Adv. Mater. Struct.*, **31**(17), 4003-4018. https://doi.org/10.1080/15376494.2023.2188326

Zheng, S., Zhang, N., Zhao, X., Chen, D. and Wang, H.T. (2024), "Size-dependent mechanical analysis of porous functionally graded piezoelectric micro/nanoscale structures: a literature review", *Smart Mater. Struct.*, **33,** 093002. https://doi.org/10.1088/1361-665X/ad5809

CC